Understanding tidal mixing at the Strait of Gibraltar: a high-resolution model approach

Nicolas M. Gonzalez, Robin Waldman, Gianmaria Sannino, Hervé Giordani, S Somot

Highlights

Understanding tidal mixing at the Strait of Gibraltar: a high-resolution model approach

Nicolas Gonzalez, Robin Waldman, Gianmaria Sannino, Hervé Giordani, Samuel Somot

- Tidal mixing mechanisms are investigated in a high-resolution simulation of the Strait of Gibraltar.

- Tidal convergence and divergence patterns, that feed recirculation cells, play an instrumental role in enhanced mixing at the Strait of Gibraltar.

- Tides drive diapycnal mixing by enhancing vertical shear and weakening vertical stratification.

- Accurate representation of both tides and abrupt topography is key for representing exchanges through the Strait of Gibraltar.

Understanding tidal mixing at the Strait of Gibraltar: a high-resolution model approach

Nicolas Gonzalez[a], Robin Waldman[a], Gianmaria Sannino[b], Hervé Giordani[a], Samuel Somot[a]

[a]*Centre National de Recherches Météorologiques (CNRM), UMR3589, Université de Toulouse, Météo-France, CNRS, Toulouse, France*
[b]*ENEA - CR Casaccia, Via Anguillarese 301, 00123 Rome, Italy*

Abstract

The Strait of Gibraltar is a narrow and shallow channel that controls the Mediterranean Sea thermohaline and biogeochemical balances. Strong tidal currents significantly modulate exchanges across this strait and induce an intense vertical mixing, impacting both the Mediterranean Sea and the Atlantic Ocean on a climatic scale. However, the turbulent processes controlling the tidal mixing location, timing, and magnitude remain unclear. To fill this gap, we investigate tidal mixing at the Strait of Gibraltar in yearly twin tidal and non-tidal simulations from a regional configuration of the three-dimensional numerical model MITgcm, using a high spatial resolution around the Strait of Gibraltar (1/200°, 100 vertical levels). More specifically, we investigate the model turbulence closure scheme, based on a turbulent kinetic energy budget, and illustrate that vertical buoyancy fluxes should be preferred to diapycnal diffusivities as mixing indicators. In agreement with previous literature, we find that tides strongly intensify vertical mixing and motions within the Strait of Gibraltar. We then demonstrate that tidal mixing relies on two main ingredients: a sustained vertical shear of horizontal velocities and a local weakening of stratification. In the Mediterranean layer, the former drives diapycnal mixing near the seafloor and the latter in shallower areas above the prominent sills of the strait. We also evidence the frequent but irregular occurrences of static instabilities in the vicinity of these sills. In the Atlantic layer, both vertical shear and stratification are involved in diapycnal mixing that develops along the trail of the eastward internal bore released at the Camarinal sill. At high frequency, the local weakening of stratification results from convergence and divergence patterns in the vicinity of the Camarinal and Espartel sills, feeding recirculation cells between the Atlantic and Mediterranean layers. In addition, we highlight that diapycnal mixing mainly develops during the westward tidal phase in the Mediterranean layer and the eastward tidal phase in the Atlantic layer. We conclude by proposing a revised conceptual view of tidal mixing at the Strait of Gibraltar, where tidally-induced recirculation cells play an instrumental role in transforming the exchanged water masses. Overall, this study emphasizes the relevance of a realistic representation of both tides and abrupt topography to simulate the exchanges through the Strait of Gibraltar and argues for the use of a specific tidal mixing parameterization otherwise.

Keywords: Ocean, modeling, Mediterranean Sea, Strait of Gibraltar, tides, mixing, Turbulent Kinetic Energy.

1. Introduction

The Strait of Gibraltar (SoG hereinafter, illustrated in Figure 1) is a narrow and shallow channel, about 15km wide at its narrowest point and 300m deep at its shallowest sill of Camarinal (CS hereinafter). It is the main connection between the Mediterranean Sea and the open Ocean. Along this approximately 60km long pathway, in the upper $\sim$ 150m depth, warmer and fresher Atlantic waters are advected into the Mediterranean Basin, whereas underneath, colder and saltier Mediterranean waters are exported to the Atlantic Ocean. This two-way exchange closes the Mediterranean Basin heat and water budgets, which, at the surface, are in deficit of $4.5 \pm 4.1 \mathrm{W.m^{-2}}$ and 0.5 ± 0.2m of annual equivalent sea level, respectively (Jordà et al., 2017). Besides the thermohaline budget, the water exchange at the SoG is also essential for the biogeochemical balance of the basin (Huertas et al., 2012), as the Atlantic inflow is one of the primary nutrient sources for the Mediterranean Sea (Ramírez-Romero et al., 2014).

Great levels of tidal energy further characterize the SoG. By interacting with ocean stratification and rough topography, tides give rise to various non-linear processes and unique mechanisms, which motivated observation campaigns in the 1980s and 1990s. At several locations across the strait, tidal currents and channel shrinkage were found to submit the flow to hydraulic control (Farmer and Armi, 1985; Farmer et al., 1988). These control points modulate the size of the volume exchanges (Bryden and Stommel, 1984) and release large internal waves, mainly toward the Mediterranean Sea (Lacombe and Richez, 1982; Wesson and Gregg, 1988; Pettigrew and Hyde, 1990), but also toward the Atlantic Ocean (Farmer et al., 1988), and across the strait (Watson and Robinson, 1990; Richez, 1994). During the Gibraltar Experiment (Bryden and Kinder, 1986), turbulence observations evidenced intense diapycnal mixing on both sides of the CS and along the trail of the eastward internal bore released at the CS (Wesson and

Email addresses: gonzalez.ni06@gmail.com (Nicolas Gonzalez), robin.waldman@meteo.fr (Robin Waldman), gianmaria.sannino@enea.it (Gianmaria Sannino), herve.giordani@meteo.fr (Hervé Giordani), samuel.somot@meteo.fr (Samuel Somot)

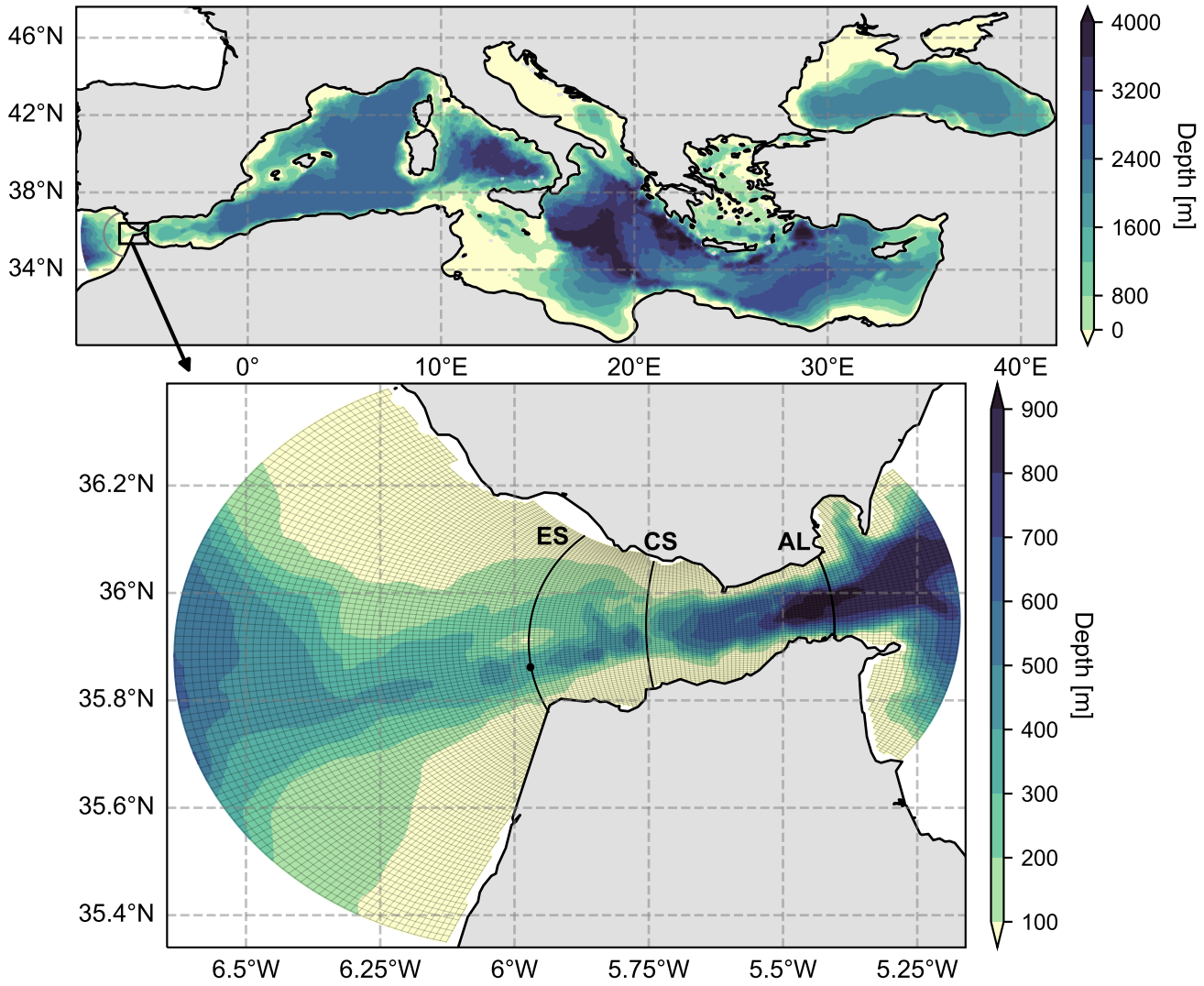

Figure 1: MITgcm model bathymetry (upper panel) and zoom on the grid and bathymetry at the SoG (lower panel). The gray line in the upper panel displays the end of the model western boundary relaxation zone. In the lower panel, meridional sections "ES", "CS", and"AL", displayed in black, refer to the Espartel Sill, the Camarinal Sill, and the entrance of the Alboran Sea, respectively. The black dot on the ES section indicates the velocity profile measurement site (INGRES project Sammartino et al., 2015).

Gregg, 1988, 1994). In addition, cross-strait hydrographic sections allowed oceanographers to examine the interface between Atlantic and Mediterranean water masses and to describe it as a distinct layer. This intermediate layer, resulting from the intense tidal mixing occurring within the strait, is advected toward the Mediterranean Sea east of the CS and toward the Atlantic Ocean west of the CS (Bray et al., 1995). It motivates the characterization of exchanges through the strait as a three-layer flow rather than an idealized two-layer flow.

More recently, high-resolution simulations using realistic physical forcing have emerged (Sannino et al., 2004, 2007; Sanchez-Garrido et al., 2011; García Lafuente et al., 2013; Sannino et al., 2014; Sanchez-Roman et al., 2018; Álvarez et al., 2019), allowing ocean modelers to reproduce and analyze in detail the main characteristics of the exchange flow through the SoG. While the eastward barotropic tide deepens and thickens the interface layer separating the Atlantic inflow from the Mediterranean outflow, the westward barotropic tide uplifts and shoals it, powering a periodic oscillation of the stratification and driving entrainment between both layers (Sannino et al., 2007; García Lafuente et al., 2013). At the CS, the interface sinking is accompanied by the relaxation of a hydraulic control point previously formed by the westward tidal currents. This hydraulic transition releases large-amplitude internal waves toward the Mediterranean Sea and produces an intense turbulent mixing (Brandt et al., 1996; Vázquez et al., 2006; Vlasenko et al., 2009; Sánchez-Román et al., 2012; García Lafuente et al., 2013; Hilt et al., 2020). Significant temperature and salinity anomalies result from this tide-induced dynamic and mixing, cooling, and saltening by up to 1°C and 0.5 psu the inflowing Atlantic water (Sannino et al., 2015).

On a larger scale, tidal influence at the SoG impacts the

Mediterranean basin-scale heat and salt budgets. By acting simultaneously on currents and thermohaline properties, tides were found to increase the net salt transport through the strait by 25% and decrease the net heat transport by 10% (Sanchez-Roman et al., 2018, Table 4 and 6). In the western Mediterranean Basin, the significant transformation of the Atlantic inflow by tidal mixing has been shown to affect the production of deep waters (Naranjo et al., 2014; Sannino et al., 2015). Over long periods (50-year simulations), Harzallah et al. (2014) reported that tides induce a general cooling (0.08°C) and saltening (0.012 psu) of the Mediterranean Sea, mainly in the upper 150m depth. In the context of global warming scenario simulations, it is essential to accurately model the SoG, which can be considered as a heat and salt anomaly filter between the Atlantic Ocean and the Mediterranean Sea (Parras-Berrocal et al., 2022; Soto-Navarro et al., 2020; Somot et al., 2006; Potter and Lozier, 2004), as well as a variable nutrient source for the Mediterranean Sea (Richon et al., 2019).

Thus, both observational and numerical studies have stressed the key role of tides in the exchanges at the SoG. However, although some aspects of tidal mixing have already been highlighted, such as variability (Wesson and Gregg, 1994; Macias et al., 2006), connection to internal waves (Wesson and Gregg, 1988; Pettigrew and Hyde, 1990; Send and Baschek, 2001; Vázquez et al., 2006) and convergence patterns within the strait (Bruno et al., 2013), the detailed mechanisms driving it remain unclear. In the literature, tidal mixing is often related to either hydraulic transitions, intensification of the vertical shear of horizontal currents, or both (García Lafuente et al., 2013; Sanchez-Garrido et al., 2011; Sannino et al., 2009; Wesson and Gregg, 1994), but no study has allowed delineating the respective importance of these phenomena throughout the strait. Other than improving our understanding of the physical mechanisms at stake at the SoG, a more extensive appreciation of tidal mixing is needed in numerical models. It would allow the development of valid alternatives to high-resolution and explicit tidal forcing at the SoG, which are often renounced in regional models of the Mediterranean Sea (Soto-Navarro et al., 2020; Harzallah et al., 2018; Llasses et al., 2018; Sannino et al., 2015; Soto-Navarro et al., 2015; Harzallah et al., 2014) because of the challenges and numerical cost associated with these developments. Recently, tidal mixing parameterizations have been developed for models that do not explicitly resolve tidal currents (de Lavergne et al., 2020). However, significant uncertainties result from the complex cascade of tidal energy to dissipation scales (Osborn, 1980; Bouffard and Boegman, 2013; Jackson and Rehmann, 2014; de Lavergne et al., 2016).

Therefore, the present work addresses the need for a deeper understanding of tidal mixing at the SoG. To this end, we analyze the processes driving turbulent mixing in ocean simulations of the Mediterranean Sea, including or not an explicit tide. Among the currently available numerical tools, we use a non-hydrostatic kilometric model resolution, which allows a faithful 3D representation of the exchange flow through the SoG and the largest internal waves at work (Hilt et al., 2020; Álvarez et al., 2019; Sannino et al., 2014). We consider that it provides an adequate framework to study the main mechanisms driving diapycnal mixing within the strait. In section 2, we introduce the model, simulations, and analysis frameworks. In section 3, we present the model validation, we characterize the effect of tides on diapycnal mixing, and we explain how it relates to tidal circulation patterns within the strait. Finally, we draw the main conclusions and discuss our results in section 4.

2. Model and methods

2.1. Model description

We use a numerical model based on the three-dimensional z-coordinate Massachusetts Institute of Technology general circulation model (MITgcm; Marshall et al., 1997a,b) adapted to the Mediterranean region. The model solves the fully non-linear hydrostatic Navier–Stokes equations under the Boussinesq approximation using a spatial finite-volume discretization. It is run with partial step topography, rescaled vertical height (z*) coordinate (Adcroft (Adcroft et al., 1997), with an implicit non-linear surface based on Campin et al. (2004). The source code and documentation are available at the following website: https://github.com/MITgcm/MITgcm (last access: 10 October 2022).

The model domain extends over the whole Mediterranean Sea and part of the Atlantic Ocean. The horizontal grid is a non-uniform and curvilinear Arakawa-C grid composed of 1040×320 points, reaching a resolution of approximately $1/200° \times 1/200°$ ($\sim$ 500m) at the SoG (Figure 1) and the Bosphorus Strait, and $1/50° \times 1/50°$ ($\sim$ 2km) at the Straits of Dardanelles. It is smoothly degraded down to a regular $1/16° \times 1/16°$ grid ($\sim$ 6km) in the Mediterranean Sea. The vertical grid comprises 100 unevenly spaced z*-levels, rescaled as suggested by Adcroft and Campin (2004). The (vertical) cell thicknesses vary between 2m at the top to 100m at the bottom. We use a time step of 20 seconds.

Three datasets compose the bathymetry: the European Marine Observation and Data Network (EMODnet) 2016 dataset (https://www. emodnet-bathymetry.eu) for the Mediterranean Basin and the Black Sea, the very high-resolution digitalized chart of Sanz et al. (1991) for the SoG, and a high-resolution bathymetry for the Bosphorus and Dardanelles Straits made available by Erkan Gökaşan (Gökaşan et al., 2005, 2007), with the permission of the Turkish Navy, Navigation, Hydrography, and Oceanography Office. The datasets were combined through a bilinear interpolation on the computational grid. In addition, a handmade check has been made for isolated points, islands, and narrow passages (see Sannino et al., 2015, 2017).
We use a third-order direct space-time flux-limited advection scheme for tracers (temperature, salinity), with a constant horizontal Laplacian diffusivity coefficient of $2 m^2.s^{-1}$. The vertical eddy viscosity and diffusivity coefficients are computed from the 1.5 order Turbulent Kinetic Energy (TKE) closure

scheme (Gaspar et al., 1990), adapted from the atmospheric case developed by Bougeault and Lacarrere (1989). The TKE scheme was chosen for its straightforward physical interpretation and its few parameters to configure. We set the background vertical eddy viscosity and diffusivity coefficients to their molecular values of $1.5 \cdot 10^{-6}\mathrm{m}^2.\mathrm{s}^{-1}$ and $10^{-7}\mathrm{m}^2.\mathrm{s}^{-1}$ for momentum and tracers, respectively. We impose a maximal diffusivity of $100\mathrm{m}^2.\mathrm{s}^{-1}$ to avoid the use of an enhanced diapycnal mixing parameterization of convection. At the lateral and bottom solid boundaries, we use no-slip conditions along with a quadratic bottom drag. The latter is calculated as a function of the velocity near the bottom, with a dimensionless coefficient of $2.5 \cdot 10^{-3}$.

2.2. Numerical simulations

We focus on two hindcast numerical simulations, differing only by the inclusion (ExpT) or omission (ExpNT) of tidal currents. The simulations are initialized with the MEDHYMAP climatology (Jordà et al., 2017) in August 1980 and run until December 31^{st} 1981.

The simulations are forced with a modified ORAS4 climatology at the Atlantic open boundary through a 3D relaxation of salinity and temperature. The relaxation time varies linearly from 2 hours at the western limit of the domain to 30 days over the first 30 grid points (gray line in the upper panel of Figure 1). Over the rest of the domain, the river runoff discharge is obtained according to Struglia et al. (2004) for the 68 main catchments and applied in conjunction with the non-linear free surface numerical scheme, see Sannino et al. (2015). The surface forcing is derived from dynamically downscaled regional atmospheric fields, produced by the Rossby Centre regional atmospheric model RCA4 (Strandberg et al., 2014), at 0.11° resolution (∼ 11km). The downscaling is performed over the EURO-CORDEX domain (Giorgi et al., 2009) with boundary conditions provided by the ERA-Interim reanalysis. Three-hourly shortwave radiation and cloud cover are directly extracted from the atmospheric model, while long-wave radiation is computed following the parameterization of Bignami et al. (1995). Three-hourly latent heat flux and sensible heat flux, and six-hourly wind stress are calculated according to the bulk formula of Large and Yeager (2004). Evaporation is computed from the latent heat. The net freshwater flux is prescribed from the net balance of evaporation, precipitation (taken from the atmospheric model), and river discharge. The model is also forced with atmospheric pressure, taken from the atmospheric model.

The explicit tidal forcing used in ExpT is the same as in Palma et al. (2020). It includes an equilibrium tide, acting as a potential in the momentum equations, and the Atlantic tide propagating from the western open boundary, where it is prescribed as an open boundary condition on the dynamic sea level. The equilibrium tide is composed of four tidal components : M2, O1, S2, K1, namely, the semidiurnal and diurnal principal lunar tides, the principal semidiurnal solar tide, and diurnal lunisolar declination tide. The tidal values used to prescribe the Atlantic tide are derived from the Oregon State University Tidal inversion software (OTIS hereinafter, Egbert and Erofeeva, 2002). In ExpNT, the equilibrium and Atlantic tides are removed.

For both ExpT and ExpNT, the first five months of simulation (01/08/1980 – 31/12/1980) are used as a spin-up for the exchange flow through the SoG to reach a steady state. At the end of the spin-up phase, we diagnose the drift of temperature and salinity over the domain defined in Figure 1 in three specific layers: the Atlantic layer (58m – 163m), the upper Mediterranean layer (163m – 371m) and the lower Mediterranean layer (371m – 670m). To do so, we fit an exponential decay to the temperature and salinity drift in each layer, and we determine their e-folding time. We find e-folding times between 20 – 40 days so that at the end of the five-month spin-up period, over 98% of the drift has occurred.
In the following, we use hourly-averaged outputs over January 1981 to perform a detailed analysis of the tidal mixing throughout a tidal cycle and yearly-averaged outputs over 1981 for an annual mean analysis. We consider that one year of simulation is sufficient to study diapycnal mixing at the SoG because the interannual variability of the transports through the strait is low compared to the tidal and subinertial variability (Boutov et al., 2014; Sanchez-Roman et al., 2018, Figures 3 and 4).

2.3. Definition of volume, heat, and salt transport at the SoG

We define the transports through the SoG in the framework of a two-way exchange flow between the Mediterranean Sea and the Atlantic Ocean. Net volume, heat, and salt transports are computed by integrating the currents, heat, and salt fluxes over a section of interest:

$$\begin{aligned}
\overline{Q_{net}}(x) &= \int_{South}^{North} \int_{bottom}^{\eta} \overline{u}\, dzdy \\
\overline{QH_{net}}(x) &= \int_{South}^{North} \int_{bottom}^{\eta} \rho_0 C_w \overline{u\theta}\, dzdy \\
\overline{QS_{net}}(x) &= \int_{South}^{North} \int_{bottom}^{\eta} \overline{uS}\, dzdy
\end{aligned} \tag{1}$$

With η the sea surface elevation, $\rho_0 = 1025\mathrm{kg.m}^{-3}$ a reference sea water density, $C_w = 3850\ J\ kg^{-1}\ °C^{-1}$ the specific heat of seawater, θ the potential temperature and S the practical salinity of seawater (as defined in the modified UNESCO formula by Jackett and Mcdougall, 1995). The overline denotes the time-average operator. Second-order terms (product of velocity with salinity or temperature) are averaged at the model time step.

Eastward and westward transports (hereinafter referred to as inflow and outflow, respectively) are more complex to estimate as they require distinguishing the two flows at high-frequency. Several definitions of the inflowing Atlantic and outflowing

Mediterranean layers have been used in the literature. In this study, we will use two different definitions, the first one to validate the simulated transports against observational-based estimates and the second to depict the full extent of the tidal influence on the water masses dynamic.

To validate the simulated transports, we follow the framework used by Sammartino et al. (2015) to estimate of the Mediterranean outflow. In this way, we define the interface between inflowing and outflowing waters as the isohaline that maximizes the outflowing volume transport (Sammartino et al., 2015, section 7.3). Due to the large amount of data required to perform this computation at high-frequency, the inflowing and outflowing transports are computed from hourly-averaged outputs over the same period as for the detailed analysis of tidal mixing, that is, January 1981. We address the uncertainty related to the time coverage of the resulting estimates in section 3. We calculate the inflows at the entrance of the Alboran Sea (AL section, see Figure 1) and outflows at the Espartel Sill (ES section), where their estimation is more robust (Jordà et al., 2017). Under this specific benchmark, we find the isohaline that maximizes the outflow to be 36.6 psu, close to the value used in (Sammartino et al., 2015; Naranjo et al., 2014), and the isohaline that maximizes the inflow to be 37.8 psu, close to the values used in (Lafuente et al., 2000; Baschek et al., 2001; Vargas et al., 2006).

To fully account for the advective properties of tides on the transports through the SoG, we refer to the framework introduced in Sanchez-Roman et al. (2018). The affiliation of a cell to a flow or the other is determined only by the sign of its pseudo-zonal velocity (model grid-oriented). In this way, we compute the inflow and outflow transports by integrating the velocities of the water masses flowing in each direction:

$$\begin{aligned} Q_{in}^{max}(x,t) &= \int_{South}^{North}\int_{bottom}^{\eta} u\, H(u)\, (x,y,z,t)\, dzdy \\ Q_{out}^{max}(x,t) &= \int_{South}^{North}\int_{bottom}^{\eta} u\, H(-u)\, (x,y,z,t)\, dzdy \end{aligned} \tag{2}$$

With H the Heaviside step function ; $H(u) = 1$ if $u > 0$; $H(u) = 0$ otherwise.
The main difference with the previous definition is that water masses from a given layer consistently flow in the same direction. Indeed, this may not be the case with the halocline interface, which allows a form of transport compensation due to the occasional presence of counter-flowing water masses in each layer. Q_{in}^{max} and Q_{out}^{max} may be considered as maximal estimates of the transport through the SoG. Note that we compute these estimates at the simulations time-step to avoid transports compensations from averaging opposite velocities.

2.4. Theoretical framework: TKE turbulent closure scheme

In a numerical model, diapycnal mixing occurs explicitly through horizontal and vertical mixing parameterizations and implicitly due to numerical discretization errors. We assume the latter source of mixing to be weak at the SoG in our simulations because of the high resolution. We have also estimated horizontal mixing using the constant horizontal Laplacian diffusivity coefficient and hourly-averaged outputs of temperature and salinity over January 1981. We found it to be, on average, five times weaker than its vertical counterpart (not shown). Therefore, we will henceforth focus on explicit vertical mixing, parameterized using vertical eddy diffusivity and viscosity coefficients (K_t and K_m, respectively), representing passive tracers and momentum diffusion by unresolved eddies. Following the mixing length theory (Prandtl, 1925), these coefficients are expressed as the product of a turbulent velocity deduced from the squared root of the TKE, a mixing length, and a mixing efficiency coefficient as follows:

$$K_m = K_t P_{rt} = c_k\, l_k\, \mathrm{TKE}^{1/2} \tag{3}$$

With :

- c_k The mixing coefficient, controlling the efficiency of turbulent mixing. Following Gaspar et al. (1990), $c_k = 0.1$.
- l_k The characteristic mixing length scale. Following Gaspar et al. (1990), $l_k = \max(10^{-9}, \min(l_u, l_d))$. l_u and l_d are introduced in Bougeault and Andre (1986), they can be interpreted as the unresolved eddies size in the upward and downward directions. In our model configuration, for a given cell, $l_u = l_d = l = \sqrt{2}\mathrm{TKE}^{1/2}N^{-1}$ as long as l does not exceed the cell thickness. Once that threshold is exceeded, $l_u = l_u^{max} \neq l_d = l_d^{max}$, where l_u^{max} and l_d^{max} depend on the upper and lower tracer cell thickness.
- P_{rt} The Prandtl number, quantifying the ratio between momentum and tracer diffusivity. $P_{rt} = \min(\max(1, 5R_i), 10)$, with R_i the bulk Richardson number that measures the ratio between the TKE destruction by stratification and its production by the vertical shear of horizontal currents. $R_i = \frac{N^2}{(\partial_z u)^2 + (\partial_z v)^2}$, where N is the Brunt-Väisälä frequency and ∂_z the partial derivative operator associated to the vertical axis.

Vertical mixing is thus defined through the TKE by the 1.5 order TKE closure scheme. This scheme resolves the TKE tendency under the assumption of horizontal homogeneity, using the dissipation parameterization of Kolmogorov (1942). It follows:

$$\begin{aligned} \partial_t \mathrm{TKE} = &\underbrace{\partial_z(K_m\, \partial_z \mathrm{TKE})}_{\text{turbulent transport } T} + \underbrace{K_m\left[(\partial_z u)^2 + (\partial_z v)^2\right]}_{\text{dynamic shear production } S} \\ &- \underbrace{K_t N^2}_{\text{buoyancy flux } B} - \underbrace{\frac{c_\epsilon \mathrm{TKE}^{3/2}}{l_\epsilon}}_{\text{dissipation } \epsilon} \end{aligned} \tag{4}$$

Where l_ϵ is the TKE characteristic dissipation length and c_ϵ an associated dissipation coefficient. Following Gaspar et al. (1990): $l_\epsilon = \max(10^{-9}, \sqrt{l_u l_d})$ and $c_\epsilon = 0.7$.
The four contributions to the TKE tendency are:

- The turbulent transport T (computed implicitly). Under the assumption of horizontal homogeneity, it represents only the convergence or divergence of the TKE vertical flux, which is parameterized using the concept of eddy diffusivity.
- The dynamic shear production S. It is always a source of TKE. Its contribution to the TKE tendency relies on the vertical eddy viscosity coefficient (inherited from the parameterization of the turbulent horizontal momentum vertical flux) and the vertical shear of horizontal velocities. On a climatological scale, S is the main source of TKE.
- The buoyancy flux B. It represents the TKE destruction (production) by the positive (negative) stratification. B also gives an estimate of diapycnal mixing as the vertical mixing tendency of tracers is equal to its convergence or divergence.
- The TKE dissipation ϵ (computed implicitly). It is always a sink of TKE. It represents the TKE destruction by molecular viscosity and is parameterized according to Kolmogorov (1942). On a climatological scale, ϵ is the main sink of TKE.

This study will mainly focus on the dynamic shear production, directly impacted by tidal forcing through vertical shear intensification or reduction. Special attention will also be paid to the buoyancy flux as a proxy for diapycnal mixing and for its ability to produce TKE in the presence of negative stratification. Note that the terms computed implicitly cannot be separated. They will be analyzed as one and referred to as the implicit TKE tendency: $I = T - \epsilon$.

3. Results

3.1. Model Validation

The tidal forcing used in ExpT has been validated over the Mediterranean Sea by Palma et al. (2020) and Sannino et al. (2015) with similar model configurations. The authors performed a one-year simulation with a barotropic version of the model and separated the tidal constituents through a harmonic analysis of the surface elevation (Foreman, 1977; Pawlowicz et al., 2002). The amplitude and phase of the modeled tides were validated against the OTIS global tide inverse model, and the simulation correctly reproduced the main zero amplitude points for the M2 tidal component in the Mediterranean Sea (Tsimplis et al., 1995). Palma et al. (2020) also validated the tidal forcing against maps from more recent tidal simulations (Ferrarin et al., 2018). In this study, we carry out further validations specific to the SoG by comparing the simulated tides to reference tidal models and observations, as well as transports and velocities against observational estimates and datasets. Regarding transports and velocities, when available, we indicate the interannual variability of the estimates. Otherwise, we provide their uncertainties, which are larger than the interannual variability of the estimated quantities.

To begin with, we will first assess the realism of the simulated tidal elevations against the observation-based charts of Candela et al. (1990) and Lafuente et al. (1990) (CA90 and GL90 hereinafter). We also refer to the global tidal atlas FES2014 (produced by Noveltis, Legos, and CLS and distributed by Aviso+, with support from CNES: https://www.aviso.altimetry.fr/) as a reference numerical dataset. In the following, differences between the charts of CA90 and GL90 provide an observational estimate of the tidal amplitude and phase. They display very similar amplitude patterns, mainly differing at the center of the strait near the Tarifa Narrow (between $5.5°W$ - $5.75°W$), where they approximately differ by 5-8cm. On the other hand, the tidal phase patterns display larger differences, peaking at the center of the strait, near the Tarifa Narrow, where they exceed $10°$. With that in mind, the amplitude and phase simulated by ExpT and FES2014 are both in good agreement with the former observations-based charts. As depicted in Figure 2, the M2 amplitude is characterized by a well-known abrupt zonal decrease from west ($\sim$ 90 cm) to east ($\sim$ 25 cm) and its phase by a meridional decrease from south to north (Lafuente et al., 1990; Candela et al., 1990). More specifically, regarding tidal amplitude, ExpT is in very good agreement with GL90, whereas FES2014 is more consistent with CA90. The zonal decrease of tidal amplitude is more intense in ExpT; however, the differences are within the range of the observation-based estimates uncertainty. Regarding the tidal phase, ExpT is in better agreement with CA90 and GL90 than FES2014. The main differences with respect to CA90 and GL90 fall within the uncertainty of the observation-based estimates.

To assess the baroclinic structure of the simulated tides, we refer to in situ Doppler current profiler measurements collected at the ES in the framework of the INGRES projects (more details in Sánchez-Román et al., 2008, 2009; Sammartino et al., 2015). We display in Figure 3 the vertical profile of M2 tidal ellipses extracted from the INGRES in situ data and the simulated velocity fields at the closest point to the measurement station. The tidal ellipses synthesize the evolution of horizontal tidal currents along the tidal cycle. Simulation-based and observation-based ellipses are in overall good agreement. They depict intense tidal currents with a dominant zonal component (up to $0.55 \mathrm{m.s}^{-1}$) of almost constant amplitude in the upper 220m depth. Below, the zonal component progressively decreases, whereas its meridional counterpart increases. The simulated zonal currents are overestimated within the upper 220m (average bias of $0.1\ \mathrm{m.s}^{-1}$), and underestimated below (average bias of $-0.06\ \mathrm{m.s}^{-1}$). Regarding the tidal phase, the simulated currents are characterized by a mean absolute phase bias of $2°$. Note that for a few ellipses, the rotation direction is reversed with respect to the observed currents (the rotating direction is indicated by "x" and "+" signs on Figure 3). However, these ellipses all depict very low meridional currents and consistent phases with respect to the observations. Thus, the rotating direction has a low impact on the associated tidal

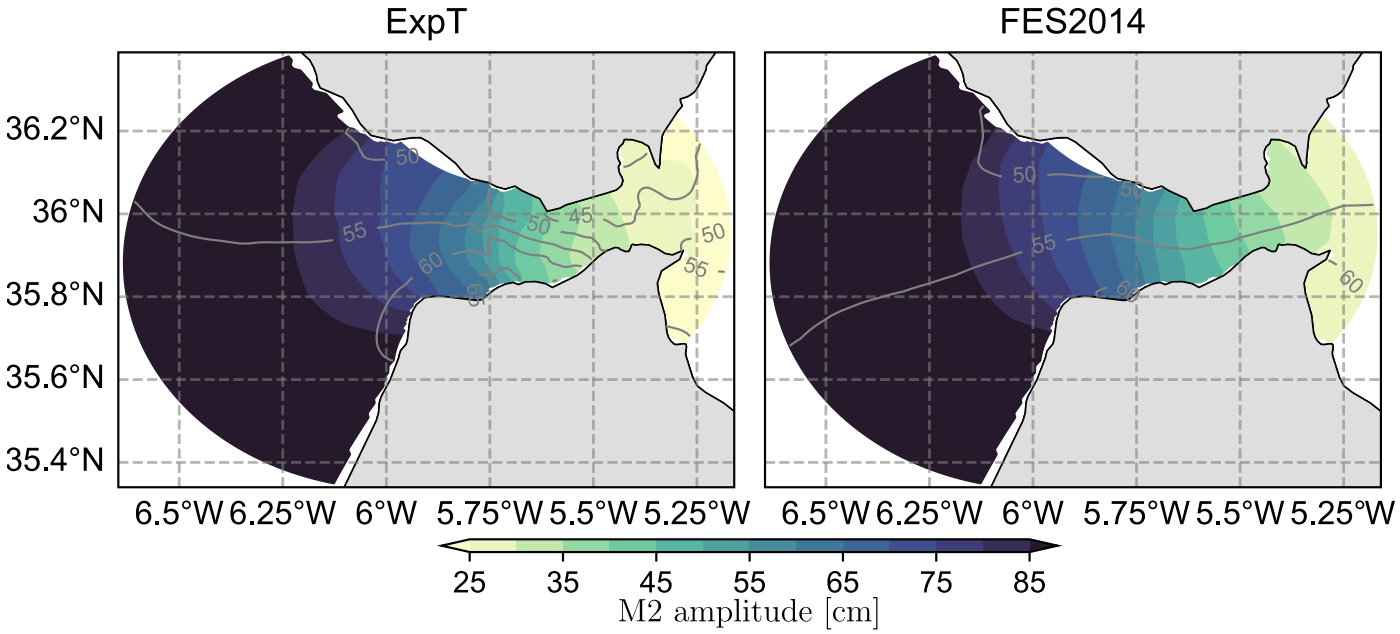

Figure 2: In shades, M2 tidal elevation amplitude, in contours, M2 tidal elevation. On the left is the MITgcm simulation, and on the right is the global tidal atlas FES2014. For ExpT, tidal amplitudes and phases are estimated from hourly outputs of instantaneous (not averaged) sea level elevation over January 1981 using the "Utide" Python package (version 0.2.5). FES2014 fields are interpolated on the MITgcm model grid through bilinear interpolation, following Xu (2018).

currents.

To conclude on the tidal validation, in light of the reasonable biases highlighted by the former analyses and the consistency with available references, we consider the simulated tides relevant to study the processes involved in tidal mixing at the SoG.

To evaluate the simulated velocities at the SoG, we refer again to in situ Doppler current profiler measurements collected in the framework of the INGRES projects. We compare 2005 – 2015 measured velocities to 1981 simulated velocities at the closest point to the measurement site (black dot in Figure 1). The results are displayed in Figure 4. For both simulations, mean velocities are in good agreement with measurements, exhibiting vertical correlation coefficients of 0.997 and 0.987, along with root-mean-square errors (RMSE hereinafter) of 0.07m.s^{-1} and 0.15m.s^{-1} for ExpT and ExpNT, respectively. The simulated currents are underestimated in ExpNT between 50m – 150m depth and overestimated in both simulations below 190m depth, with a notable improvement in ExpT. With respect to measurements, the zero-velocity interface only differs by $\sim$ 10m, with a notable improvement in ExpT. As expected, the non-tidal simulation largely underestimates the zonal velocity variability at high-frequency. With respect to INGRES measurements, the hourly standard deviation of zonal velocity depicts a RMSE of 0.29m.s^{-1}, with a minimal amplitude at 220m depth, just below the mean zero-velocity interface. The addition of tidal forcing substantially corrects this bias, decreasing the RMSE to 0.09m.s^{-1} in ExpT. Consistently with the results from the tidal validation, ExpT overestimates the variability of zonal velocities over the upper 220m depth and underestimates it below.

Table 1 summarizes the main characteristics of transports through the SoG. To be as consistent as possible with observations, we calculate the inflows (outflows) at the AL (ES) section, where their estimation is more robust (Jordà et al., 2017) (see Figure 1). For both ExpT and ExpNT, the computed volume inflow and outflow fall within the confidence interval of Jordà et al. (2017, Table 3) and the estimation interval of Sammartino et al. (2015) for sub-annual timescales, respectively. Although simulations estimates are only computed over January 1981, their consistency over longer periods can be assessed by considering the monthly variability of the Mediterranean outflow as an uncertainty range. The latter is estimated at 0.08Sv by Sammartino et al. (2015). Note also that the computed heat and salt transport are within the range of the values commonly obtained with similar numerical models (Jordà et al., 2017). Regarding the net transports (computed over 1981, at the CS, although they are uniform throughout the strait), the volume and heat transports are consistent with the accepted range defined by Jordà et al. (2017). For the salt transports, the simulations are out of the indirect estimate range from Jordà et al. (2017). However, they remain relatively close to it, given its high uncertainty and the high sensitivity of net salt transports to interannual variations of the inflow and outflow.

The effect of tidal forcing is evident in the maximal transport estimates $Q^{\max}$. For ExpT, $Q^{\max}$ displays large values, twice as high as $\overline{Q}$, whereas for ExpNT, $Q^{\max}$ and $\overline{Q}$ are relatively similar. This reflects that tidal forcing induces intense high-frequency variations of zonal advection, which is consistent with water mass recirculation and periodic reversals

		Volume: $\overline{Q}$ ($Q^{\max}$) [Sv]	Heat: $\overline{QH}$ [$W.m^{-2}$]	Salt: $\overline{QS}$ [$10^6 kg.s^{-1}$]
IN_{AL} 1981/01	ExpT	0.81 (1.63)	19.3	29.4
	ExpNT	0.79 (0.87)	19.3	28.6
	Jordà et al. (2017), Table 3	0.86±0.10	-	-
OUT_{ES} 1981/01	ExpT	-0.86 (-1.45)	-18.4	-32.6
	ExpNT	-0.86 (-0.96)	-18.14	-32.72
	Sammartino et al. (2015)	-0.85±0.08	-	-
NET_{CS} 1981	ExpT	0.06	4.77	0.68
	ExpNT	0.06	5.00	0.55
	Jordà et al. (2017)	0.04±0.02	4.5±4.1	0.1±0.3

Table 1: Average pseudo-zonal transports of volume, heat, and salt for the MITgcm model simulations ExpT and ExpNT. AL, CS, and ES stand for the Alboran, Camarinal Sill, and Espartel Sill sections, respectively (see Figure 1). The inflow and outflow (in Sverdrups) are computed over January 1981 from hourly outputs at the AL and ES sections (Figure 1), respectively. Net transports are computed over 1981 at the CS section (Figure 1). For the volume transports, we indicate an alternative, maximal estimate in brackets, which accounts for high-frequency flow variations over 1981. When available, references are given in the third row. As traditionally done for comparison purposes with surface forcing, we convert the heat flux into an equivalent surface flux over the whole Mediterranean Sea, in $W.m^{-2}$, considering the Mediterranean area to be $2.5 \cdot 10^{12} m^2$, following Sanchez-Roman et al. (2018).

of the exchange flow (Candela et al., 1990; Bryden et al., 1994; Lafuente et al., 2000). These results are in line with Sanchez-Roman et al. (2018), who highlighted that inclusion of tidal forcing intensifies the exchanges through the SoG, however, to a much lesser extent. The substantial values highlighted here can be attributed to the computation of $Q^{\max}$ at the simulation time-step, in contrast to the use of 3-hourly averages in Sanchez-Roman et al. (2018), which allows transports compensations from averaging opposite velocities. Tidal forcing also influences the net heat and salt transport through the strait, which decreases by 5% and increases by 24% in ExpT, respectively. These modifications are similar to what is reported in Sanchez-Roman et al. (2018). It is important to note that they are significant, especially for the net salt transport, whose observed estimate is, however, highly uncertain (Jordà et al., 2017). In longer simulations, such changes would likely impact the heat and salt contents of the Mediterranean Basin after a few years of integration.

3.2. Characterization of Tidal Mixing Within and Around The SoG

Several studies have already investigated the impact of tidal forcing on the currents and water masses at the SoG (Sanchez-Roman et al., 2018; Sannino et al., 2015; Naranjo et al., 2014; Harzallah et al., 2014). The following discussion reinforces the results highlighted in these studies and gives further details on the tidal mixing intensity and location.

Figure 5 displays the model mean temperature, salinity, westward and eastward velocity, vertical eddy diffusivity coefficient, and absolute vertical buoyancy flux, averaged along the model pseudo-meridional direction for the domain illustrated in Figure 1. In panels (a) and (b), we can readily distinguish the relatively warm and fresh Atlantic layer ($\sim$ 15°C – 17.5°C and 36 psu – 37 psu), flowing toward the Mediterranean Sea, from the cold and salted Mediterranean layer ($\sim$ 13°C – 14°C and 37.5 psu – 38.5 psu), flowing toward the Atlantic Ocean. The zero-velocity interface separating these two layers (black line in Figure 5) is almost flat within the strait, around 150m depth, and sinks to 300m depth to the west, following the Mediterranean outflow. At fixed depths, the water masses depict noticeably different characteristics along the strait, indicating the occurrence of intense diapycnal mixing and water masses recirculation. This is particularly striking near the depth of the inflowing and outflowing layers interface, where temperature and salinity vary by up to 1°C and 1 psu along the strait. Comparison with ExpNT reveals that tides induce intense temperature and salinity anomalies within the strait (colored contours in Figure 5 (a) and (b)). These anomalies organize as vertical dipoles, indicating a vertical redistribution of heat and salt. Regarding temperature, tides significantly cool the surface above 50m depth, especially east of the CS, where mean temperature anomalies reach −0.5°C. Underneath, Atlantic and Mediterranean water masses are warmed less intensely (up to +0.3°C). Note that the temperature dipole is not centered on the interface between the inflowing and outflowing layers, as it results from the impact of tides on the warm ocean surface in summer. At that time, tidal motions mainly flux heat to depth, cooling the top fifty meters by up to −1°C and warming less intensely the water masses below (not shown). Regarding salinity, the tide-induced anomalies provide a vivid picture of diapycnal mixing and vertical displacement of the interface between Mediterranean and Atlantic water masses (Figure 5 (b)). Above the velocity interface, mean salinity increases by up to 0.2 psu, whereas below, it decreases by up to 0.15 psu.

The mean westward and eastward velocities (Figure 5 (c) and (d)) illustrate the remarkable intensity of the exchange

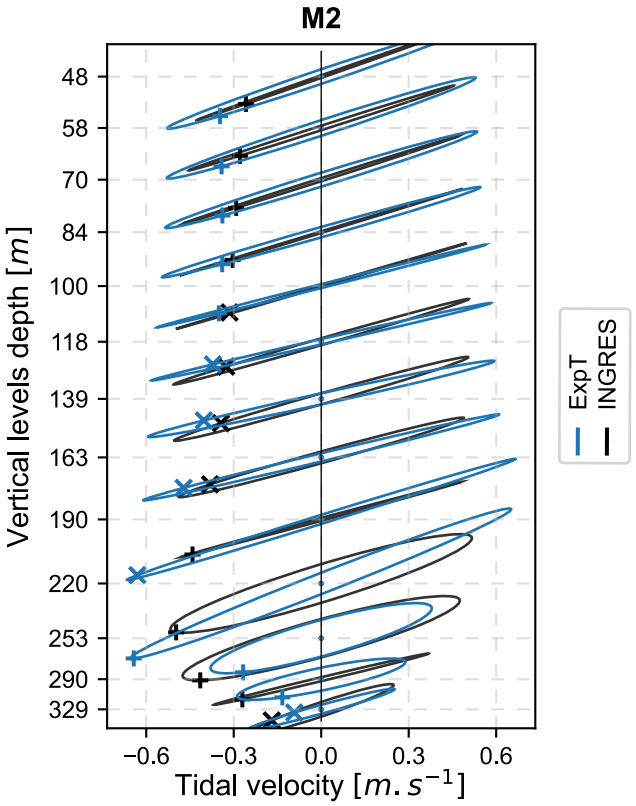

Figure 3: Vertical profile of tidal ellipses associated with the M2 horizontal tidal currents. In blue, MITgcm simulation (ExpT), in black, in situ Doppler current profiler measurements from the INGRES project. The y-scale is adjusted to preserve an equal proportion between zonal (along the x-axis) and meridional (along the y-axis) currents. The location of the current vector at the zero Greenwich phase is indicated by the symbols "+" and "x". The rotation direction of current vectors is clockwise for the ellipses marked with the symbol "x" and counterclockwise for those marked with the symbol "+". Tidal ellipses parameters are computed using the "Utide" Python package (version 0.2.5) from hourly-averages of horizontal currents, taken the closest point to the measurement site ($\simeq$ 35.86°N, 5.97°W; black dot in Figure 1), over January 1981 for ExpT, and instantaneous 30-minute measurements over January 2004-2015 for the INGRES dataset. For ExpT, horizontal velocities are obtained by projecting the model outputs onto the zonal and meridional directions. Measurements are linearly interpolated onto the model vertical grid.

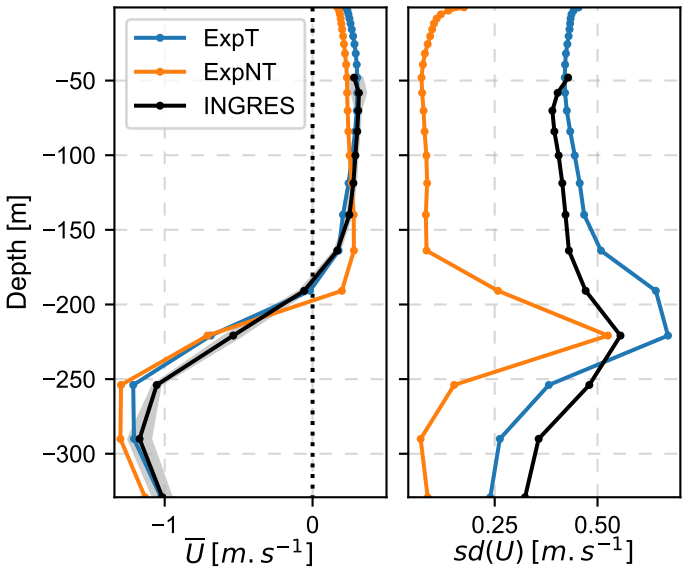

Figure 4: Mean (left) and hourly standard deviation (right) of the zonal velocity profile at the Espartel Sill (see Figure 1). In black, 2005 – 2015 mean in situ Doppler current profiler measurements from the INGRES project, with a sampling interval of 30 minutes (Sammartino et al., 2015). Dark shades represent the interannual variability computed from the measured data. In blue and orange, 1981 mean simulated zonal velocity, taken at the closest point to the measurement site ($\simeq$ 35.86°N, 5.97°W; black dot in Figure 1), for ExpT and ExpNT, respectively. The zonal velocities are obtained by projecting the model outputs onto the zonal direction. Measurements are linearly interpolated onto the model vertical grid.

flow through the SoG, as well as the intense vertical shear that characterizes it. After crossing the CS, the Atlantic and Mediterranean layers become narrower, forcing the water masses to accelerate up to 1 m.s^{-1}. Overall, tidal forcing increases both eastward and westward advection (colored contours in Figure 5 (c) and (d)), reflecting a periodic reversal of the inflowing and outflowing layers (Candela et al., 1990; Bryden et al., 1994; Lafuente et al., 2000). Local decreases in the velocity fields can be explained by tidal recirculation patterns above the main topographic obstacles of the strait (Sanchez-Roman et al., 2018). In this way, the weakening of westward currents at the crest of the CS and west of the ES is consistent with the recirculation of the Mediterranean outflow. Given the reduction of the ExpT near-bottom velocity bias at the ES with respect to INGRES measurements (Figure 4), this suggests that tidal currents act as a mitigator of the zonal Mediterranean jet intensity. Conversely, the local intensification of westward velocities between the CS and ES is consistent with Atlantic water recirculation, also evidenced by the decrease of eastward velocities above 100m depth east of the CS.

The vertical eddy diffusivity coefficient (Figure 5 (e)) is averaged at each time step of the simulation before no-slip conditions modify it. It is, thus, fully defined by the TKE closure scheme and the wind stress at the surface (used as a boundary condition for the TKE). At the SoG, vertical diffusivities reach a maximum near the seafloor. They are also noticeably strong, although to a lesser extent, above 50m depth, between 50m – 300m depth just east of the CS, and near the zero-velocity interface. Overall, tides mainly influence eddy diffusivities near the seafloor, where they modify the stratification and the vertical shear of horizontal currents (Equations 3 and 4). Given the intense temperature and salinity anomalies above 300m depth (Figure 5, (a) and (b)), the former analysis reveals that the vertical eddy diffusivity coefficient is not adequate to draw an accurate picture of diapycnal mixing, although it is commonly used to do so (Sannino et al., 2015, Figure 11). Indeed, eddy diffusivities can be seen as a measure of the tracer gradient diffusion rate, and thus, they must be interpreted in conjunction with the background stratification. A good illustration is that for a given level of turbulence (TKE$_{ref}$), the eddy diffusivity coefficient is more intense in well-mixed areas than in strongly stratified areas ($K_t \propto \text{TKE}_{ref} N^{-1}$ in Equation 3). Conversely, in this scenario, diapycnal mixing increases

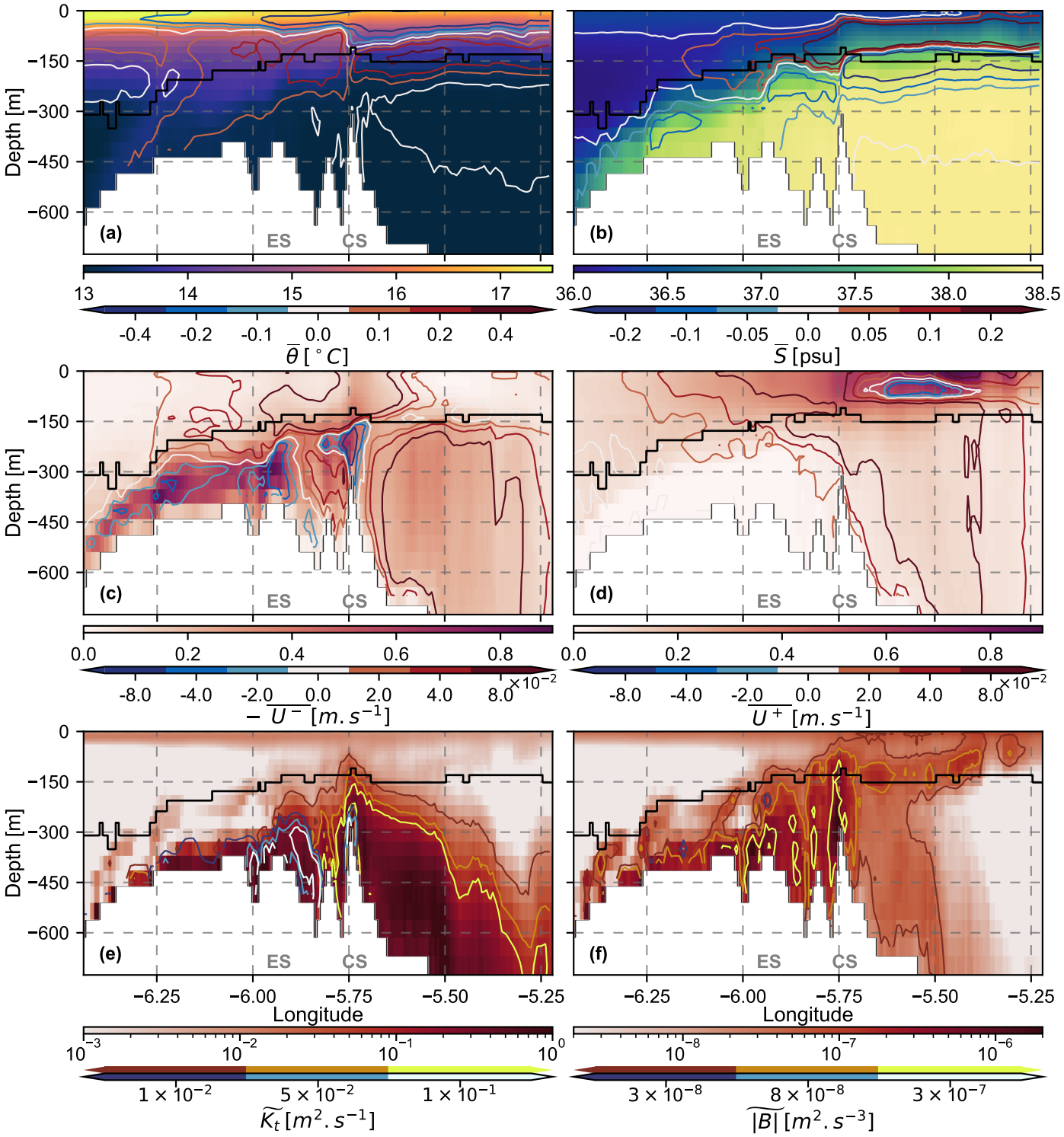

Figure 5: From (a) to (f): Model 1981 mean temperature, salinity, eastward velocity U^+, westward velocity U^-, vertical eddy diffusivity coefficient K_t, and absolute vertical buoyancy flux $|B|$ in ExpT (shades). The fields are spatially averaged over pseudo-latitudes (following the model grid) of the domain illustrated in Figure 1, excluding coastal areas (shallower than 100m depth). Anomalies with respect to ExpNT (ExpT-ExpNT) are represented in contours, with colors defined according to the lower color bars below the figure. For panels (e) and (f), in which we use a logarithmic scale, negative anomalies are indicated in dark to light-blue shades and positive anomalies in brown to yellow shades. The black line marks the 1981 average interface depth between the inflowing Atlantic waters and outflowing Mediterranean waters. It is defined in a vertical integral sense as follows: $\text{argmax}_{d\in[0;bot]} \int_d^0 \bar{U}\, dz$. The acronyms "ES" and "CS" in gray refer to the Espartel Sill and the Camarinal Sill, respectively. The mean eddy diffusivity coefficient and buoyancy flux are geometrically averaged over pseudo-latitudes to filter out isolated large values and highlight the most meridionally-consistent patterns using the following operator: $log_{10}\left(\widetilde{X}\right) = \frac{\int log_{10}(X)\, dzdy}{\int dzdy}$. Note that the illustrated seafloor represents the maximum of the model bathymetry. Thus, bottom anomalies related to shallower regions may appear a few hundred meters above

with stratification. In the following, we will use the absolute buoyancy flux $|B|$ as a measure of diapycnal mixing since it accounts for both diffusivity and stratification (Equation 4) and relates directly to the tracer mixing trends. We consider the absolute value to capture the total amount of diapycnal mixing, whether it is produced in the presence of stable ($N^2 > 0$) or unstable ($N^2 < 0$) stratification.

As expected, $|B|$ is intense in areas of strong vertical shear (Figure 5 (f)), such as the upper 50m, above the seafloor, and near the zero-velocity interface. It also reaches high values east of the CS in the Atlantic layer, between the zero-velocity interface and the surface, reflecting the occurrence of turbulent mixing. $|B|$ is minimal west of $6°W$ below 50m depth in the Atlantic layer and east of $5.5°W$ in the Mediterranean layer, respectively. This indicates that both water masses experience turbulent mixing upon crossing the CS. East of the CS above the seafloor, the buoyancy flux is moderate despite the intense viscosity (Figure 5 (e)). It illustrates that in weakly stratified areas, high diffusivities do not reflect strong diapycnal mixing. Tides mainly strengthen $|B|$ above the CS up to the surface, between the CS and ES in the Mediterranean layer, at the bottom of the Atlantic layer east of the CS, and to a lesser extent, at the eastern flank of the CS (colored contours in Figure 5 (f)). These intensification patterns are consistent with enhanced mixing near the seafloor and between the Atlantic and Mediterranean layers, as well as the incorporation of recirculating water masses within each layer. However, differences with respect to tidal temperature and salinity anomalies (Figure 5 (a) and (b)) suggest that the latter mainly reflects the periodic vertical advection of the interface between both layers.

Figure 6 illustrates the vertical average of $|B|$ over the same domain as the one considered in Figure 5. It gives a horizontal perspective on the diapycnal mixing intensity and location. Once again, the CS stands out as a location of intense buoyancy fluxes. Further west, $|B|$ is enhanced by the Mediterranean outflow, which drives vertical shear and turbulent mixing near the bottom. At the eastern side of the strait, the vertical average of $|B|$ is much lower (with respect to the west) due to the absence of solid obstacles on the path of the Atlantic jet. As expected, tides intensify diapycnal mixing within most of the strait, except along the Mediterranean outflow pathway, where both increased and reduced mixing are evident (Figure 5 (e)).

Thus, the addition of tidal forcing leads to significant changes in the mean characteristics of the exchange flow through the SoG. Analysis of vertical buoyancy fluxes indicates that diapycnal mixing substantially increases within the strait, and provides insight into its location and intensity. However, investigation of the related mechanisms is limited by the analysis of long-term averages, which depict large residual anomalies from periodic reversals of the exchange flow and vertical displacements of the Atlantic and Mediterranean water masses. This emphasizes the need to investigate the tidal dynamics and associated mixing at high-frequency.

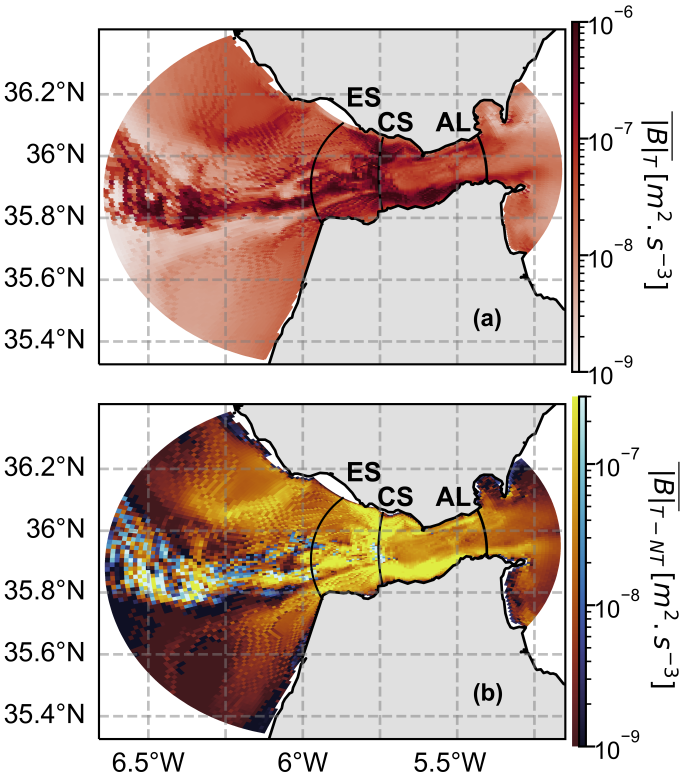

Figure 6: Depth average absolute vertical buoyancy flux $|B|$ in 1981 from ExpT (a), and anomalies with respect to ExpNT (b) (ExpT-ExpNT). Because of the logarithmic scale, negative anomalies are indicated in dark to light-blue shades and positive anomalies in brown to yellow shades. The acronyms "ES", "CS", and "AL" in black refers to the Espartel Sill, the Camarinal Sill, and the entrance of the Alboran Sea, respectively.

3.3. Insight Into Turbulent Mixing at the SoG

In the previous section, we have detailed the effect of tides on water masses and currents at the SoG. We have then related these effects to diapycnal mixing patterns. We will now investigate the processes driving diapycnal mixing within the strait by analyzing TKE production ($\partial_t TKE > 0$) and destruction ($\partial_t TKE < 0$) at high frequency. We assume here that a large production of TKE reflects the occurrence of diapycnal mixing. Indeed, the increase of TKE is a necessary condition for the occurrence of intense diapycnal mixing (not a sufficient condition, as the buoyancy flux $B \propto TKE\ N$; Equations 3 and 4).

Figure 7 displays the evolution along the tidal cycle of the TKE tendency terms, integrated between ES and AL sections (Figure 1). The considered period starts at spring tides and ends at neap tides in order to capture the influence of the fortnightly tidal cycle on the TKE. As expected, the dynamic shear production (S) and the implicit TKE tendency ($I = T - \epsilon$, representing the terms of the TKE prognostic equation computed implicitly) are the dominating terms of the tendency (Figure 7, upper panel). Both share the same order of magnitude and follow similar variations, reaching their maximum during spring tides and their minimum during neap tides. Note that the integral of I is always negative

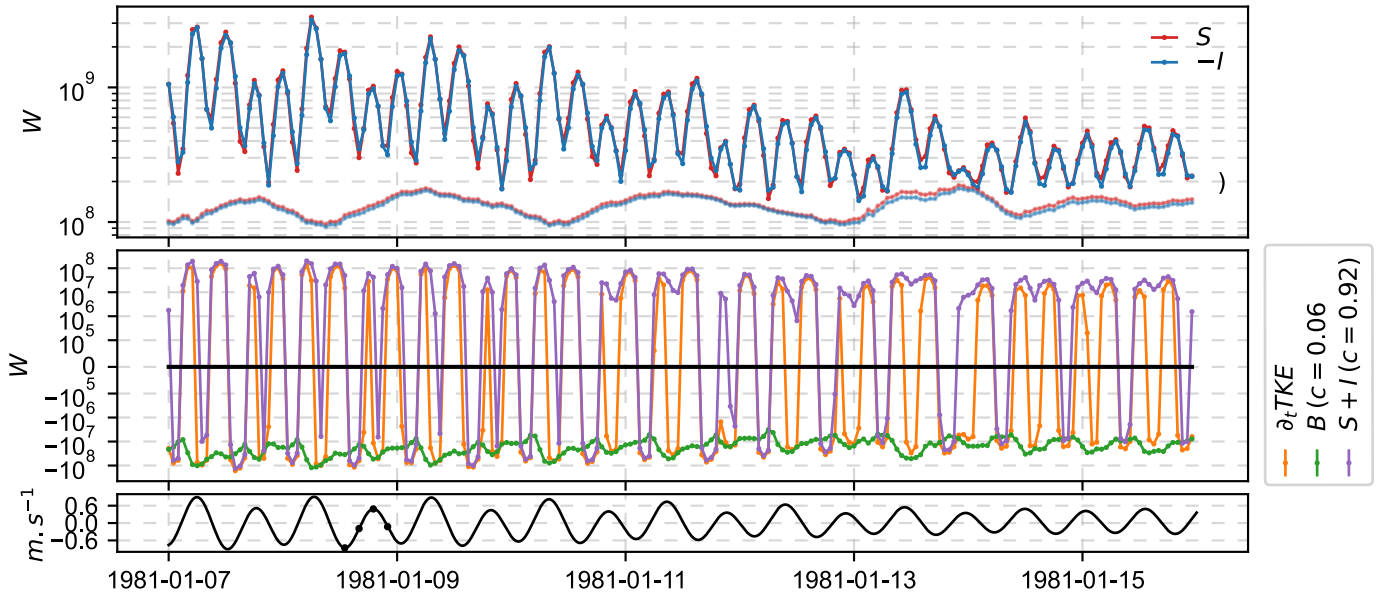

Figure 7: Hourly time series of the TKE tendency terms integrated between ES and AL sections (Figure 1) in ExpT. The period considered includes spring tide (01/07 – 01/12) and neap tide (01/12 – 01/16). The upper panel illustrates the dynamic shear production (in red) and the terms of the TKE prognostic equation computed implicitly (in blue, it includes TKE dissipation, vertical transport, and boundary conditions). The light-colored lines show the value of these terms in ExpNT. On the middle panel, we display the total tendency of TKE (in orange), the buoyancy flux (in green), and the sum of dynamic shear production and implicit TKE tendency (in purple). The correlation coefficient with the total tendency is given in the legend. The lower panel illustrates the pseudo-zonal (following the model grid) barotropic tidal currents, estimated from the simulated pseudo-zonal and pseudo-meridional velocities, using the "Utide" Python package (version 0.2.5). The four black dots represent the time of the hourly averages displayed in Figures 9 and 10

over the domain and period examined. It indicates that TKE dissipation is the main contributor to I. Overall, the inclusion of tidal forcing substantially enhances S and I. Consistently with observations from Wesson and Gregg (1994), at hourly frequency, tides induce large oscillations in the intensity of S and I, reflecting a periodic intensification of the TKE and, thus, the occurrence of diapycnal mixing. To investigate the source of this tide-induced turbulence, we can look at the respective contributions of the TKE tendency terms. The buoyancy flux B (Figure 7, middle panel), always negative, is less variable and less intense than S and I. It correlates poorly with the total tendency (correlation coefficient of 0.06), which may be surprising since we have just described B as a good indicator of diapycnal mixing. However, it is essential to remind that B is related to the TKE and thus, not directly to its tendency. In fact, the poor correlation between B and the TKE tendency only suggests that B does not drive it but may occasionally alter it. On the contrary, the sum of I and S depicts a strong correlation with the TKE tendency (coefficient of 0.92), which points out that within the strait, the main drivers of TKE are dynamic shear production and dissipation.

In order to identify the physical mechanisms driving the TKE intensification through S, we will first shed light on the conditions required to trigger TKE production. Let us consider an initial state before the emergence of turbulence. We can argue that stratification is strong with respect to the TKE such that mixing and dissipation length scales are defined by: $l_k = l_\epsilon = l = \sqrt{2}N^{-1}\mathrm{TKE}^{1/2}$ (l is lower than the cells thickness). Focusing on the terms able to create or dissipate TKE, we can write from Equations 3 and 4:

$$\partial_t \mathrm{TKE} - T = \sqrt{2}N^{-1}\mathrm{TKE}\left(c_k \mathrm{Sh} - N^2\left(\frac{c_k}{P_r} + \frac{c_\epsilon}{2}\right)\right) \quad (5)$$

with Sh the squared vertical shear of horizontal currents. Thus, the balance between TKE production and dissipation only depends on vertical shear and vertical stratification (N^2). Going further in this argument, we can show (Appendix A, Equation A.2) that TKE production is triggered when the bulk Richardson number decreases below a critical value $R_{i_c} \simeq 0.23$, close to the value commonly used to indicate the development of Kelvin-Helmholtz instabilities: $R_g = 0.25$ (Fernando, 1991). Simply put, for turbulence to develop, the vertical stratification must be sufficiently weak relative to the vertical shear of horizontal currents. We can conclude that tide-induced turbulence at the SoG must rely on either a local weakening of stratification or an intensification of vertical shear, or both.

To determine which of the former processes drives TKE production, we display in Figure 8 (a-b) the 1981 mean pseudo-meridional average correlation coefficient of the dynamic shear production S with the vertical shear Sh and vertical stratification N^2. Since the variables of interest vary exponentially and the function relating them is not linear, we investigate their correlation using the Spearman rank correlation coefficient (Schober et al., 2018). The results reflect a strong correlation between S and Sh within most of the strait. However, in areas where S is high (black contour in Figure 8), the correlation decreases as we move away from the seafloor. Conversely, N^2

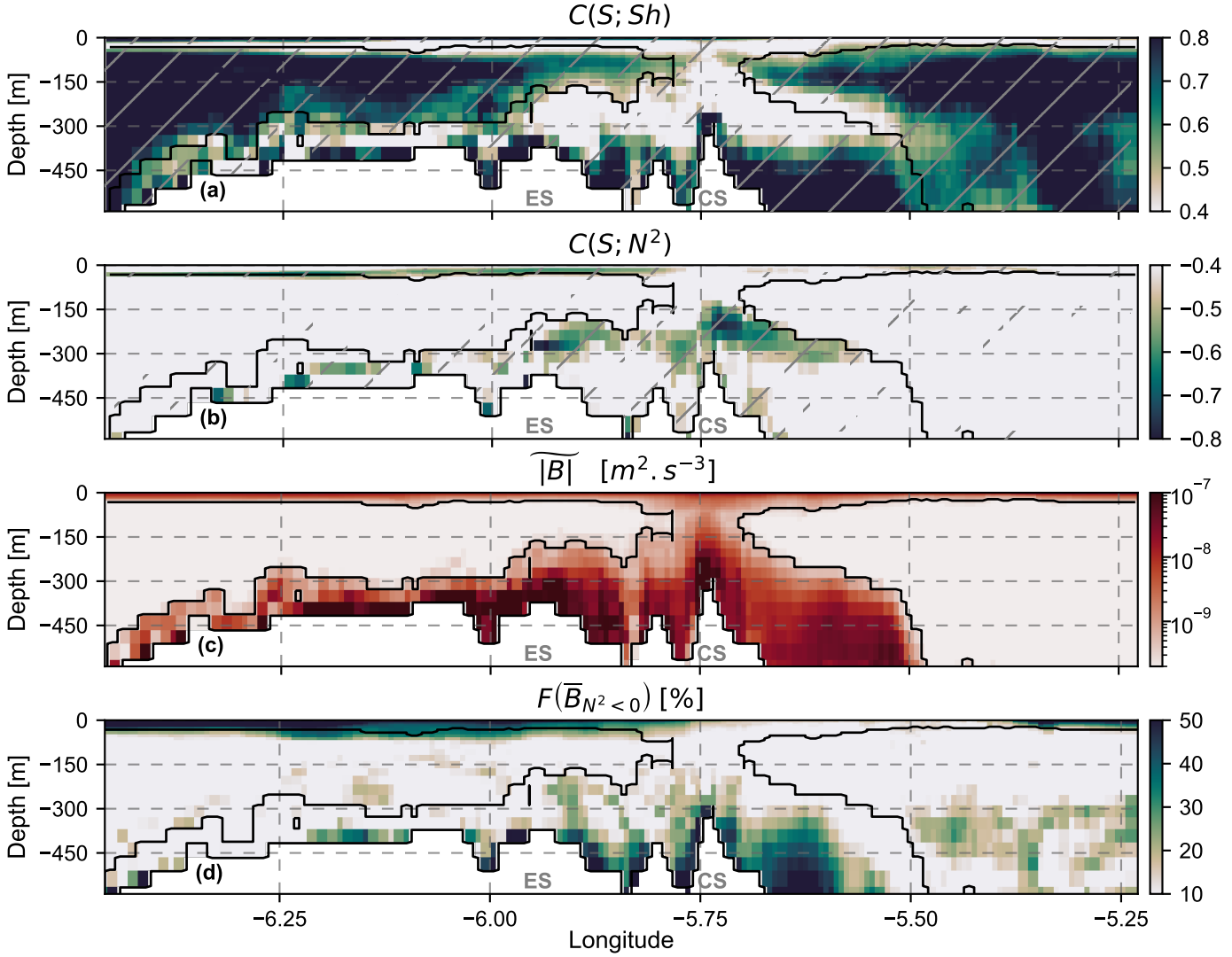

Figure 8: Panels (a) and (b) represent the pseudo-meridional average (following the model grid) Spearman rank correlation coefficient of dynamic shear production (S) with the squared vertical shear of horizontal currents (Sh) and stratification (N^2), respectively. Hatches mark areas where the correlation significance level is above 95% according to Student's T-test. Panels (c) and (d) show the time and pseudo-meridional geometric average of the absolute vertical buoyancy flux $|B|$ and the fraction of buoyancy flux oriented downward, respectively. Black contour lines delimit areas where dynamic shear production is consistently intense over time (i.e., where its time and pseudo-meridional geometric average is greater than 2 10^{-9}m^{2}s^{-3}). We use hourly outputs over 1981/01/01 – 1981/02/01 to compute time averages and correlation coefficients. The spatial domain considered is represented in Figure 1. The acronyms "ES" and "CS" refer to the Espartel Sill and the Camarinal Sill, respectively (see Figure 1).

depicts significant negative correlation patterns in these areas, particularly above topographic obstacles, and a poor correlation over the rest of the strait. Note that the correlation patterns of N^2 and Sh do not fully overlap, leaving areas where both are low. At these locations, we can deduce that N^2 and Sh equally contribute to the generation of vertical mixing. Thus, the former analysis emphasizes that although vertical shear drives TKE production in moderately turbulent areas, its influence in energetic areas is confined to the seafloor as stratification plays a greater role at shallower depths. In this way, tidal mixing at the SoG relies not only on an intensification of vertical shear by tidal currents but also on the work these currents exert against vertical stratification.

In order to relate TKE production to diapycnal mixing, we now investigate the buoyancy flux generated at the SoG and its relation to TKE production. To focus on areas where the buoyancy flux is consistently strong, we display in the panel (c) of Figure 8 the absolute buoyancy flux pseudo-meridional geometric average in 1981/01, representing the temporal and spatial average of its order of magnitude. As previously hypothesized, a significant buoyancy flux develops in areas of intense TKE production, namely, along the path of Mediterranean outflow west of the CS, above the CS, and east of the CS above 60m depth and below 300m depth. Between 150-300m depth above the main topographic obstacles, where stratification drives the TKE, the intense buoyancy flux indicates that TKE production is strong enough to induce diapycnal mixing, even if stratification has weakened ($B \propto TKE\ N$). Thus, stratification weakening acts as a trigger, allowing turbulence

to develop and eventually produce diapycnal mixing.

An alternative mechanism to that described in Equation 5 is the generation of static instabilities ($N^2 < 0$), which result from the advection of dense water over lighter water. In this scenario, the conditions for TKE production change as the characteristic mixing lengths reach their threshold values ($l_k^{max} \neq l_\epsilon^{max}$). It can be shown (Appendix A, Equation A.1) that TKE production then requires the vertical shear and/or the (negative) stratification to be sufficiently strong, relatively to the TKE: $\frac{c_k}{c_\epsilon} l_k^{max} l_\epsilon^{max} \left(\mathrm{Sh} - N^2\right) >$TKE. Thus, either (negative) stratification, vertical shear, or both can power great diapycnal mixing. To investigate this mechanism, we display in panel (d) of Figure 8 the pseudo-zonal average fraction of downward buoyancy flux over January 1981. Over the top 50m depth west of $5.75°W$, and close to the seafloor, a significant fraction of the buoyancy flux is oriented downward (at least 20%). In low turbulence areas, occasional static instabilities can account for a large fraction of the mean buoyancy flux. However, in areas of intense TKE production, such as near the seafloor between $6.25°W$ and $5.5°W$, the significant fraction of downward buoyancy flux suggests the frequent occurrence of large static instabilities. Since stratification does not strongly correlate with S in this area, we can assume that these instabilities act as an unsteady mixing source of variable intensity and location. Such mechanism is consistent with the unstable structures observed by Farmer et al. (1988, Figure 13.1) and Wesson and Gregg (1994) near the crest and the west flank of the CS, respectively. On the other hand, the absence of significant negative buoyancy flux above 300m east of the CS indicates that diapycnal mixing mainly develops in a stably stratified sheared flow there.

3.4. Tidal Recirculation Patterns

We have just shown that besides vertical shear, tidal mixing at the SoG relies on the local weakening or reversal of stratification, suggesting the presence of strong tidal recirculation patterns within the strait. We will now describe these patterns throughout a tidal cycle and investigate how they relate to diapycnal mixing. Although not discussed in this section, the mixing induced by horizontal eddy diffusion is briefly investigated in Appendix B.

Figures 9 and 10 show the evolution of practical salinity (panels (a)), absolute buoyancy flux (panels (b)), circulation (panels (a) and (b), arrows), and absolute buoyancy flux variations with respect to the previous tidal phase (panels (c) and (d)) throughout different tidal phases on 1981/01/08. Namely, we display in Figure 9 the peak of the outflowing phase and the rise of the inflow, and in Figure 10 the peak of the inflowing phase and the rise of the outflow. In each panel, we also display isopycnals to track deeper density variations. Panels (d) specify the mechanism driving absolute buoyancy flux variations. This diagnostic is based on the detection of meridionally consistent variations of stratification and vertical shear. It relies on the hypothesis that TKE drives hourly buoyancy flux variations ($B \propto \mathrm{TKE}\,N$; see Appendix D). The reader wishing to examine buoyancy flux and stratification variations is referred to the annex Figures C.14 and C.15, which also display a budget for the stratification tendency.

Throughout all periods illustrated in Figures 9 and 10, fresher Atlantic waters are readily distinguishable from saltier Mediterranean waters (panels (a)). The large zonal variations of salinity along the strait (up to 2psu near 150m depth) indicate the occurrence of diapycnal mixing and vertical advection associated with water masses recirculation. These are more directly reflected by intense buoyancy fluxes (panels (b)) and significant volume transport variations (upper line plots panels). In the course of the tidal cycle, absolute buoyancy flux variations (panels (c)) depict an alternation of intense and moderate mixing phases, with a 6-hour phase lag between the inflowing and outflowing layers. In moderately turbulent areas, these variations are mainly driven by the vertical shear of horizontal currents (panels (d)). In energetic areas, the complex mechanisms at play ask for a more detailed analysis.

At the peak of the outflow (Figure 9 (1), 1 p.m.), westward advection greatly intensifies, and the Atlantic inflow reverses between $6.25 - 5.50°W$. On the other hand, the Mediterranean outflow reaches the CS with high velocity, where it is blocked and forced to diverge. This is evidenced by an intense upwelling of dense water masses against the CS (the 1029 isopycnal locally shoals up to $\sim$ 150m depth) and a meridional transport from the center of the strait towards the land (not shown). The diverging water masses mainly converge west of the sill, where they force intense downward currents, completing the mechanism described in Bruno et al. (2013). East of the CS, the divergent flow forces surface Atlantic and intermediate Mediterranean water masses to flow toward the Mediterranean Sea. Following Sanchez-Roman et al. (2018), the resulting structure may be described as a vertical recirculation cell, identifiable by an intensification of volume transports east of the CS (upper panel of Figure 9 (1)). During this first tidal phase, diapycnal mixing is mainly intensified in the upwelled Mediterranean layer. West of the CS, this intensification results from vertical shear strengthening above the seafloor. On the contrary, above and east of the CS, as vertical shear diminishes with respect to the previous tidal phase, it is the stratification weakening by vertical tidal advection that allows diapycnal mixing to develop. Diapycnal mixing is also enhanced by static instabilities near the crest of the CS, consistently with observations from Farmer et al. (1988, Figure 13.1), and at the eastern flank of the sill.

At the rise of the inflow (Figure 9 (2), 4 p.m.), the Mediterranean outflow intensity diminishes but maintains the recirculation cell previously described. East of the CS, the $1028.8\mathrm{kg.m}^{-3}$ isopycnal flattens and rises above 150m depth, reflecting a shoaling and widening of the tongue of upwelled Mediterranean waters. In addition, the intensified eastward advection forces the upwelled water masses to flow toward the

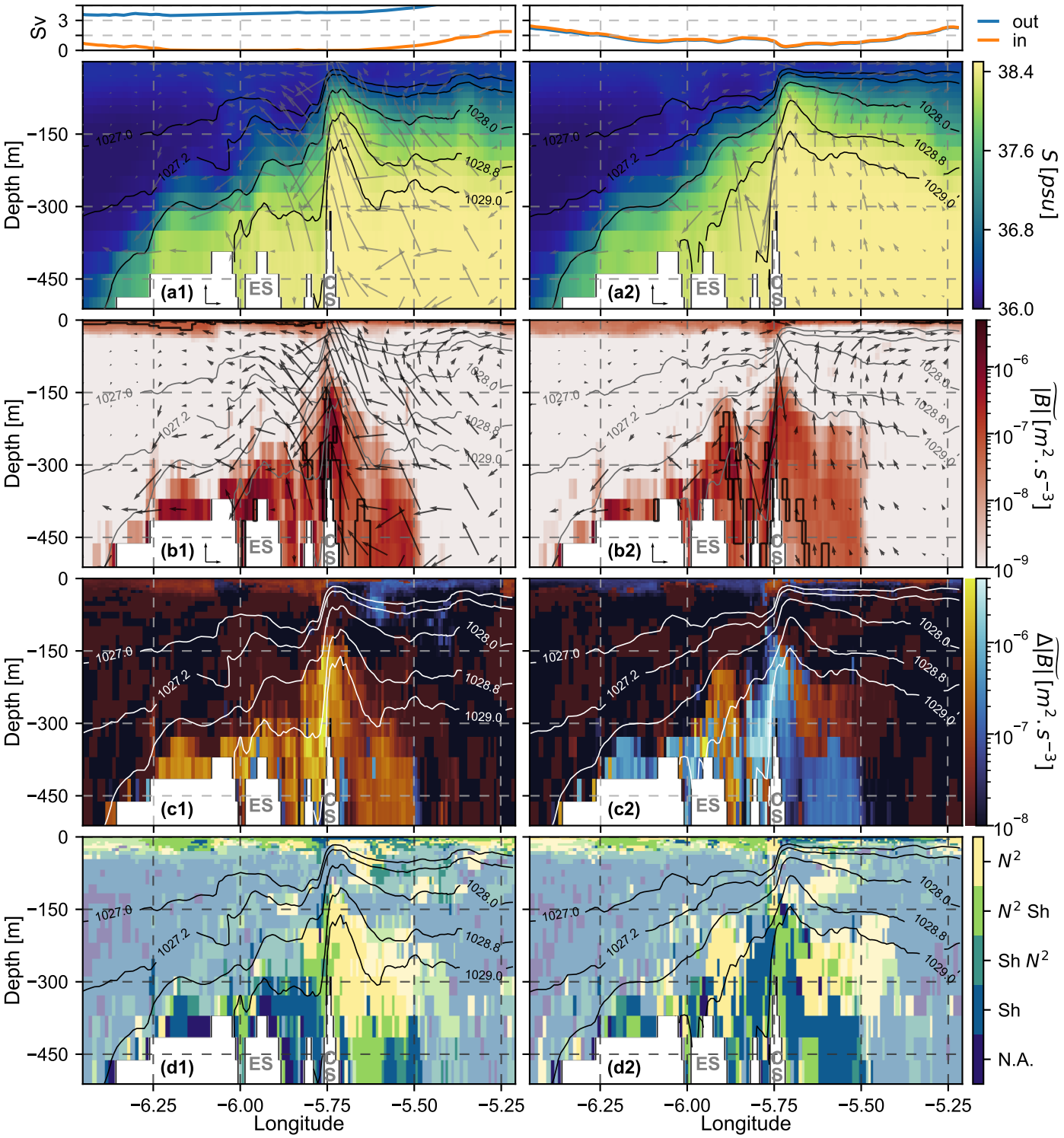

Figure 9: In shades, from top to bottom: pseudo-meridional average (following the model grid) (a) practical salinity, (b) absolute vertical buoyancy flux $|B|$, (c) $|B|$ variation with respect to the previous tidal phase (three hours before), and (d) processes driving $|B|$ variations. The colors of panels (d) stand for stratification (N^2), both stratification and vertical shear, with a dominant influence for stratification (N^2 Sh) or vertical shear (Sh N^2), vertical shear (Sh), and non-identified process (N.A., see Appendix D for further details). The fields are hourly-averaged outputs, extracted on 1981/01/08 at 1 p.m. (1), 4 p.m. (2) (black dots in Figure 7). The top blue and orange line plots represent the westward and eastward volume transport (in Sverdrups), respectively, computed from hourly-averaged outputs of zonal velocity. In panels (a) and (b), arrows represent the velocity direction and norm. Reference arrows are displayed next to the image labels, representing a vertical and pseudo-zonal velocity of 0.005m.s^{-1} and 0.5m.s^{-1}, respectively. Black contours in panels (b) outline areas where the average of the buoyancy flux is oriented downward and the absolute buoyancy flux higher than 5 10^{-8} m^2.s^{-3}. The 1027kg.m^{-3},1027.2kg.m^{-3}, 1028kg.m^{-3}, 1028.8kg.m^{-3}, and 1029kg.m^{-3} isopycnal surfaces are illustrated in contours for all panels. For panels (d), areas where the absolute buoyancy flux variations are lower than 2.5 10^{-8} m^2.s−4 in absolute value are made transparent. The acronyms "ES" and "CS" in gray refer to the Espartel Sill and the Camarinal Sill, respectively (see Figure 1). Time and spatial averages of the buoyancy flux are performed as detailed in Figure 5. For $\Delta|B|$, the meridional average only considers the cells driving meridionally dominant variations (see Appendix D).

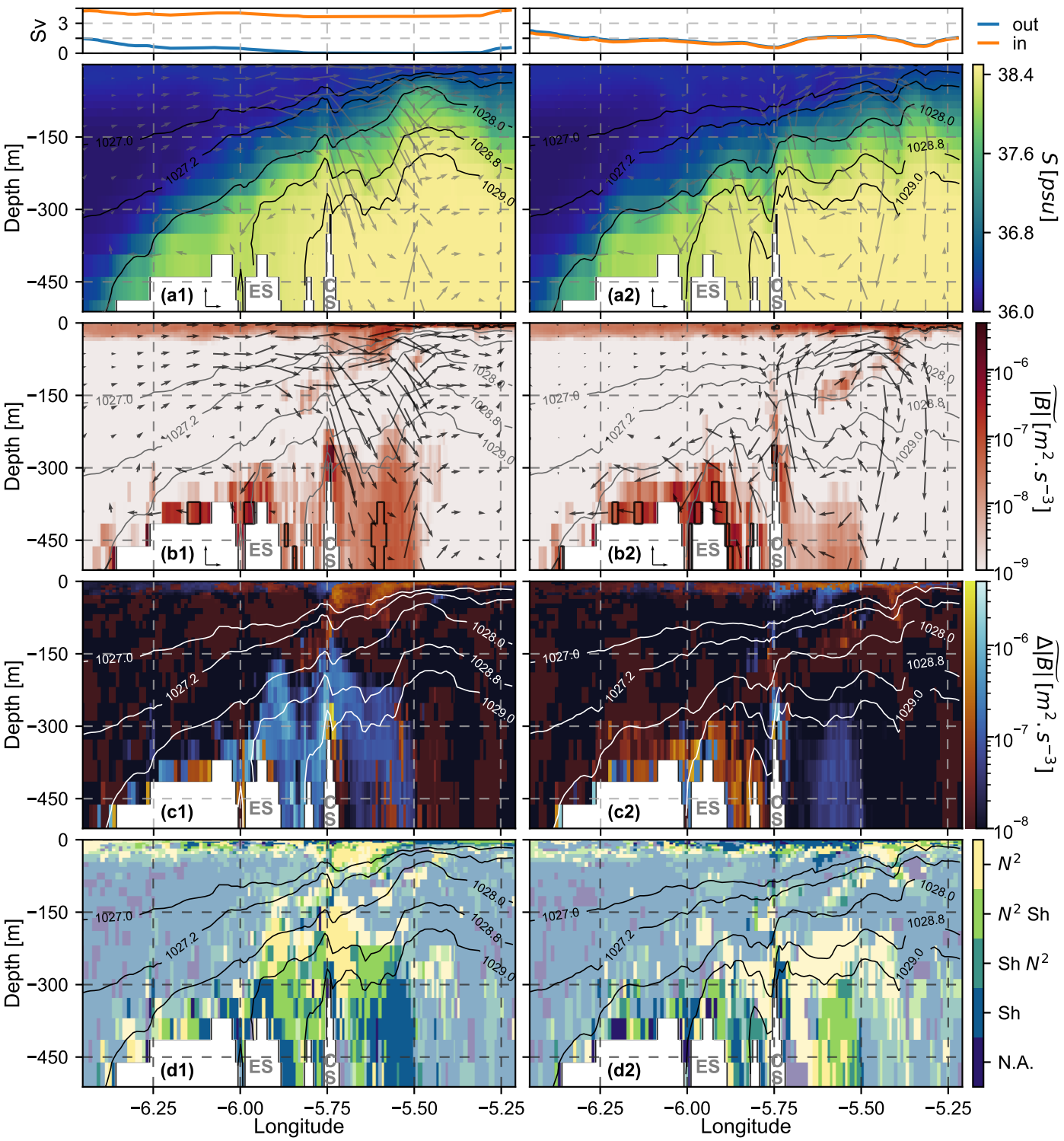

Figure 10: Same as Figure 9 for hourly outputs extracted at 7 p.m. (1) and 10 p.m. (2) (black dots in Figure 7).

Alboran Sea, marking the release of the well-known internal bore at the CS (Ziegenbein, 1969, 1970; Farmer et al., 1988; Richez, 1994; Morozov et al., 2002). West of the CS, the intensified Atlantic inflow maintains the convergence area above the CS and partially recirculates along the western flank of the sill. This recirculation pattern is, to some extent, closed at the ES by a less intense recirculation of outflowing water masses. The overall structure is evidenced by a local increase in volume transports between the ES and CS. During this intermediate tidal phase, with respect to the outflowing phase, diapycnal mixing has reduced above the seafloor as vertical shear progressively diminishes, and tidal advection restores the stratification near the CS. Conversely, diapycnal mixing intensifies between $\sim$ 300 − 150m depth east of the ES and the CS, where upward and westward advection weakens the stratification. Above the ES, the turbulence is further enhanced by the occurrence of static instabilities, which may be related to the unstable structures observed by Wesson and Gregg (1994) and simulated by various numerical models (Hilt et al., 2020; García Lafuente et al., 2013; Sanchez-Garrido et al., 2011).

At the peak of the inflowing phase (Figure 10 (1), 7 p.m.), the recirculation cells east of the CS and ES vanish as the Mediterranean outflow reverses. West of the CS, intense eastward tidal currents continue to force water mass convergence toward the center of the strait, as evidenced by the active Atlantic recirculation cell. The internal bore released during the previous tidal phase propagates eastward, and the inflowing Atlantic water masses following it restore stratification. Diapycnal mixing is significantly reduced in the Mediterranean layer. Indeed, above and around the CS, the deepening of the Atlantic layer increases stratification and, thus, prohibits diapycnal mixing. In addition, on both sides of the CS, the reduced vertical shear above the seafloor allows for a less intense mixing to develop. Conversely, diapycnal mixing intensifies in the thickened Atlantic layer east of the CS, where stratification weakens and vertical shear intensifies in the trail of the released bore.

At the rise of the new outflowing phase (Figure 10 (2), 10 p.m.), eastward advection diminishes but retains enough intensity to maintain the convergence area west of the CS, where the Atlantic inflow partly recirculates. On the other hand, the intensified Mediterranean outflow is forced to diverge against the eastern flank of the CS, forming the previously described recirculation cell. Further east, the internal bore propagates toward the Alboran Sea. The convergence area that follows it produces an intense recirculation opposing that on the eastern flank of the CS. Smaller waves develop along the trail of the internal bore. Among these structures, the vertical velocity dipole between $5.75 - 5.50°W$ indicates the propagation of a second-mode internal wave, observed by Farmer et al. (1988); Vázquez et al. (2006). These waves power a moderate diapycnal mixing in the Atlantic layer and at the interface with the Mediterranean layer through their local influence on vertical shear and stratification. In the Mediterranean layer, diapycnal mixing vanishes between $5.75 - 5.50°W$ due to the strengthening of stratification by vertical currents. Conversely, west of the CS, diapycnal mixing intensifies as the vertical shear increases with the Mediterranean outflow intensity.

Overall, these results explicitly reveal the tidal recirculation patterns at SoG and their connection to diapycnal mixing. They highlight that besides vertical shear near the seafloor, tidal mixing at the SoG strongly relies on the upwelling of dense Mediterranean water masses against the CS, favoring TKE production at the top of the Mediterranean layer, where stratification weakens, and producing an internal bore in the Atlantic layer, which locally weakens stratification and enhances vertical shear .

3.5. Synthetic mechanism

Although the exact location and intensity of diapycnal mixing at the SoG are highly variable, in this section, we propose a synthetic view of the different steps driving its occurrence in the course of the tidal cycle (Figure 11).

We consider an initial state in which the interface between the Atlantic and Mediterranean layers is relaxed (dashed line in Figure 11 (1)). As in ExpNT, it is smoothly slanted downward toward the Atlantic, characterized by an intense vertical shear, but also a strong stratification, such that $R_i > R_{i_c}$ and limited mixing occurs. Let us now consider the action of the outflowing tide on the system (solid line in Figure 11 (1)). East of the CS, the local upwelling of Mediterranean waters forms a recirculation cell between the Atlantic and Mediterranean layers. Stratification locally weakens above the CS, favoring TKE production and diminishing its dissipation (Equation 4). Once stratification is low enough relative to the vertical shear of horizontal currents ($R_i < R_{i_c}$), turbulence develops, progressively strengthening diapycnal mixing. As long as strong vertical shear persists, the recirculation cell continuously powers diapycnal mixing on the top of the Mediterranean layer by extracting available potential energy from the upwelled Mediterranean water masses. Diapycnal mixing also develops near the seafloor, where the Mediterranean outflow intensifies the vertical shear.

During an intermediate tidal phase (Figure 11 (2)), eastward velocities increase, whereas westward velocities progressively diminish. Above the seafloor, the intense diapycnal mixing progressively decreases as the Mediterranean outflow slows down. Similarly, diapycnal mixing diminishes above the CS, where the vertical shear decreases, and the released eastward internal bore restores the stratification. Just west of the CS, the convergence of water masses induces a second recirculation cell. The latter transports relatively light Atlantic water masses deeper into the Mediterranean layer west of the CS, where static instabilities form. These unstable structures further enhance diapycnal mixing, which is powered by the upwelling of dense water masses against the ES.

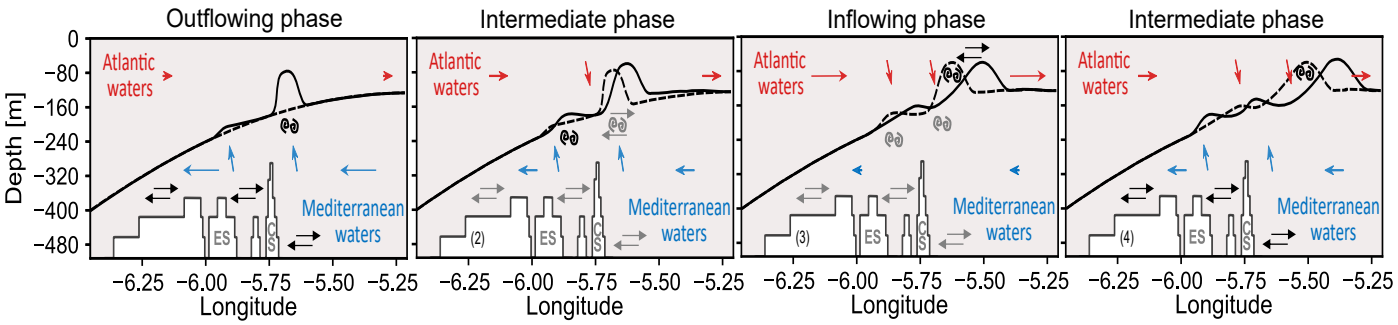

Figure 11: Synthetic schematic of tidal mixing at the Strait of Gibraltar. Advection of Atlantic and Mediterranean waters is indicated with red and blue arrows, respectively. Diapycnal mixing is illustrated by opposite horizontal arrows when driven by vertical shear, by spirals when driven by stratification, and a combination of these symbols when driven by both. Black symbols reflect the occurrence of intense diapycnal mixing. Gray symbols indicate a significant but decreasing diapycnal mixing. Acronyms "ES" and "CS" in gray refer to the Espartel Sill and the Camarinal Sill, respectively (see Figure 1). The interface between the Mediterranean and Atlantic layers is indicated by the solid (current location) and dashed lines (previous location). The idealized scenario starts in panel (1) with a relaxed interface between the Mediterranean and Atlantic layers. The interface is then deformed during the outflowing tidal phase (solid line), and diapycnal mixing develops in the Mediterranean layer where stratification weakens and vertical shear intensifies. During the intermediate (panel 2) and inflowing tidal phases (panel 3), diapycnal mixing progressively diminishes in the Mediterranean layer and increases in the Atlantic layer. In panel (4), during a final inflowing phase, diapycnal mixing continues to develop in the Atlantic layer along the trail of the eastward internal bore.

During the inflowing tidal phase (Figure 11 (3)), east of the CS, the recirculation cell vanishes due to the low intensity of the Mediterranean outflow. Above the CS, in the Mediterranean layer, stratification is restored, and diapycnal mixing is inhibited. Specifically, TKE shear production decreases while dissipation increases, reversing the TKE tendency (Equation 5). Conversely, east of the CS, the weakened stratification and intensified vertical shear along the trail of the internal bore allow the development of diapycnal mixing in the Atlantic layer.

During a last intermediate tidal phase (Figure 11 (4)), eastward velocities decrease, whereas westward velocities progressively intensify. Diapycnal mixing continues to develop along the trail of the internal bore. Over time, the internal bore disintegrates into smaller waves, which may produce further mixing by modifying the local stratification and vertical shear. Above the seafloor, diapycnal mixing increases as the vertical shear progressively strengthens with the Mediterranean outflow.

This synthetic view stresses the instrumental role of tidal recirculation cells and internal waves released at the CS in powering diapycnal mixing at the Strait of Gibraltar.

4. Conclusions and Discussions

This study characterizes tidal mixing at the Strait of Gibraltar (SoG hereinafter), a key phenomenon controlling water mass transformations across the strait. To do so, we analyze and compare twin tidal and non-tidal yearly MITgcm simulations over the Mediterranean Sea, with high-resolution at the SoG ($1/200°$, 100 vertical levels). Our analysis focuses on mechanisms driving explicit vertical mixing, defined by the 1.5-order turbulent kinetic energy closure scheme. We strongly emphasize that eddy diffusivity coefficients are irrelevant for measuring such mixing, which is better depicted by the vertical buoyancy flux.

The simulated tides are in good agreement with available observation-based references. In addition, both tidal and non-tidal simulations compare well to velocity measurements at the Espartel Sill (ES hereinafter) and transport estimates through the strait, with a notable improvement of the simulated velocities in the tidal simulation. As expected, tidal currents strengthen diapycnal mixing and induce considerable recirculation patterns across the strait, which are controlled by the main topographic obstacle: the Camarinal Sill (CS hereinafter). On an annual scale, tidal hydrographic anomalies mainly result from water mass recirculation and vertical displacements of the interface between the Atlantic and Mediterranean layers. East of the CS, the upper 150m depth, advected on average toward the Mediterranean sea, are cooled by up to 0.5°C and saltened by up to 0.2 psu. On the contrary, west of the CS, the water masses below 150m, flowing on average toward the Atlantic Ocean, are warmed by up to 0.2°C and freshened by up to 0.15 psu. Regarding the net transports, tide-induced currents and mixing decrease the net heat transport through the SoG by 5% and increase the net salt transports by 24%, which is consistent with the results reported in Sanchez-Roman et al. (2018, Table 4 and 6). In agreement with the previous literature (Naranjo et al., 2014; Harzallah et al., 2014; Sannino et al., 2015), these results further highlight the significant influence of tides on the thermohaline exchanges through the SoG. They emphasize the relevance of modeling tidal currents at the SoG for the thermohaline balances of the Mediterranean Basin and, to a lesser extent, the Atlantic Ocean.

Investigation of diapycnal mixing shows it is intense above the seafloor throughout the strait and in the Atlantic layer east of the CS. Tides substantially strengthen diapycnal mixing within the strait, particularly west of the CS above the seafloor, above the CS up to the surface, and east of the CS in the Atlantic layer. We then investigate the Turbulent Kinetic Energy (TKE)

scheme to identify the mechanisms of tidal mixing at the SoG. As expected, it reveals that the vertical shear of horizontal currents drives TKE production near the seafloor. However, at intermediate depths above the main topographic obstacles, turbulence is mainly driven by modulations of the stratification. It then relies on two mechanisms:

- Stratification weakening in areas of strong vertical shear of horizontal currents, particularly near the interface between the Atlantic and Mediterranean layers; this condition is reached when the bulk Richardson number, which measures the ratio between vertical stratification and shear, decreases below a critical value: $R_{i_c} \simeq 0.23$.
- The reversal of stratification, which mainly occurs in the Mediterranean layer close to the main topographic obstacles, due to water masses recirculation.

At shallower depths, in the Atlantic layer, diapycnal mixing is powered by eastward internal waves released at the CS through their impact on stratification and vertical shear.

Finally, we relate these mechanisms to circulation patterns within the strait. We show that the diapycnal mixing intensifies during different tidal phases for the Mediterranean and Atlantic layers, with a 6-hour time lag. In the Mediterranean layer, diapycnal mixing intensifies during the outflowing tidal phase, when vertical advection weakens stratification, and westward advection increases vertical shear near the seafloor. In the Atlantic layer, mixing intensifies during the inflowing tidal phase. It develops along the trail of the eastward internal bore of upwelled Mediterranean water masses released at the CS, where stratification locally weakens and vertical shear intensifies. Consistently with Sanchez-Roman et al. (2018), these results emphasize that water mass transformations throughout the SoG strongly rely on vertical tidal motions at the CS. In addition, we explicitly show tidal recirculation cells between the Atlantic and Mediterranean layers, and large static instabilities near the main topographic obstacles of the strait.

As a further step in understanding tidal mixing at the SoG, this study would gain from comparison with a very-high-resolution non-hydrostatic counterpart, allowing to investigate the role played by high-order internal wave baroclinic modes, which are a key component of the energy cascade over abrupt topography (Lahaye et al., 2020). Although the mechanisms highlighted in this study should remain consistent, fine-scale and non-hydrostatic features, such as short internal solitary waves formed along the trail of the eastward internal bore released at the CS, should affect the intensity and location of diapycnal mixing (Hilt et al., 2020; Álvarez et al., 2019; Sannino et al., 2014). Such study could also assess the consistency of the highlighted recirculation cells to the relaxation of the hydrostatic assumption. Regarding turbulence closure schemes, a similar work based on an alternative scheme to that of the TKE (Umlauf and Burchard, 2005) would be very instructive. In particular, the use of 3D turbulence schemes would allow assessing the consistency of the classical horizontal homogeneity assumption at increasingly high resolution.

In the meantime, this study emphasizes the key role that both tides and abrupt topography play in controlling the exchanges at the SoG. In addition to tidal forcing, accurate representation of the seafloor, in particular the CS, appears as a necessary condition to resolve tidal mixing. Similarly, the magnitude of the fine-scale mechanisms suggests that a kilometric model resolution is also essential. Hence, our results question the reliability of coarse numerical models in representing the exchange flow through the SoG, even when tides are explicit (Harzallah et al., 2014). Regarding tidal mixing parameterizations, the magnitude of diapycnal mixing at the SoG is unlikely to be matched by current parameterizations, which present a significant energy loss in high turbulence regimes due to water column homogenization assumptions under energetic regimes (de Lavergne et al., 2016). However, these results should not stand in the way of improving such parameterizations, which are a low numerical cost alternative for non-tidal and low-resolution simulations. For example, implementing a specific tidal mixing parameterization for the SoG could be the key to notable improvements in the modeling of the Mediterranean Sea and the Atlantic Ocean at climatic scales. To this aim, the simple parameterization introduced in Sanchez-Roman et al. (2018) would be a promising start.

Regarding observational validation, so far, past field measurements have been too scarce to validate the modeled tidal mixing mechanism. However, multiple observational campaigns at the SoG have shown large vertical displacements of the interface between the Atlantic and Mediterranean layers, as well as deep Mediterranean water suction above the strait, all related to the tidal cycle (Farmer and Armi, 1985; Farmer et al., 1988; Kinder and Bryden, 1990; Wesson and Gregg, 1994; García Lafuente et al., 2002; Sánchez-Román et al., 2012). In light of these observations, the mechanisms highlighted in this study are reasonable. Their field investigation would require microstructure turbulence measurements, together with hydrographic and velocity measurements at the SoG, throughout the main semidiurnal tidal cycle.

Finally, it is worth noting that the results highlighted in this study may be transferable to other straits of the world, provided that they include shallow sills and are subject to strong tidal currents.

Data availability

Data and codes are available from the first author upon request.

Acknowledgements

This work is part of the Med-CORDEX initiative (www.medcordex.eu) and in particular of the CORDEX Flagship Pilot Study on an improved representation of small-scale

oceanic processes and air-sea coupling in the region climate system models (CORDEX FPS-airsea).

Appendix A. On the conditions for TKE production

In this appendix, we derive from the TKE tendency equation necessary and sufficient conditions for the production of TKE. Consistently with our simulations, we consider the following numerical parameters: $c_k = 0.1$; $c_\epsilon = 0.7$; $P_r = \max(1, \min(10, 5R_i))$; $R_i = \frac{N^2}{(\partial_z u)^2+(\partial_z v)^2}$. Also, we refer to the squared vertical shear of horizontal currents as Sh.

We search for a condition for the production of TKE. From Equation 4, we have:

$$\begin{aligned} &\partial_t \mathrm{TKE} - T \geq 0 \\ \Rightarrow\ & c_k l_k \mathrm{TKE}^{1/2}\mathrm{Sh} - c_k l_k \mathrm{TKE}^{1/2}\frac{N^2}{P_r} - c_\epsilon \frac{TKE^{3/2}}{l_\epsilon} \geq 0 \\ \Rightarrow\ & c_k l_k \mathrm{TKE}^{1/2}\left(\mathrm{Sh} - \frac{N^2}{P_r}\right) - c_\epsilon \frac{TKE^{3/2}}{l_\epsilon} \geq 0 \\ \Rightarrow\ & \frac{c_k}{c_\epsilon} l_k\, l_\epsilon \left(\mathrm{Sh} - \frac{N^2}{P_r}\right) \geq TKE \end{aligned} \tag{A.1}$$

We must now distinguish two cases, depending on whether the mixing and dissipation length scales have reached their threshold values or not. In the latter case (i.e. $l_k = l_\epsilon = \sqrt{2}N^{-1}TKE^{1/2}$):

$$\begin{aligned} &\frac{c_k}{c_\epsilon} 2\left(\mathrm{Sh}N^{-2} - \frac{1}{P_r}\right) \geq 1 \\ \Rightarrow\ &\frac{c_k}{c_\epsilon} 2\left(\frac{1}{R_i} - \frac{1}{P_r}\right) \geq 1 \end{aligned}$$

From the definition of the Prandtl number, we distinguish three conditions:

- if $R_i \geq 2$ (i.e. $P_r = 10$) :

$$\frac{c_k}{c_\epsilon} 2\left(\frac{1}{R_i} - \frac{1}{10}\right) \leq \frac{c_k}{c_\epsilon} 2\left(\frac{1}{2} - \frac{1}{10}\right) < 1$$

- if $2 > R_i > 0.2$ (i.e. $P_r = 5R_i$) :

$$\begin{aligned} &\frac{c_k}{c_\epsilon} 2\left(\frac{1}{R_i} - \frac{1}{5R_i}\right) \geq 1 \\ \Rightarrow\ &\frac{c_k}{c_\epsilon} 2\frac{4}{5} = R_{i_c} = 0.23 \geq R_i \end{aligned}$$

- if $R_i \leq 0.2$ (i.e. $P_r = 1$) :

$$\frac{c_k}{c_\epsilon} 2\left(\frac{1}{R_i} - 1\right) > 8\frac{c_k}{c_\epsilon} > 1$$

Finally:

$$\begin{aligned} &\partial_t \mathrm{TKE} - T \geq 0 \\ &\Rightarrow R_i \leq R_{i_c} \end{aligned} \tag{A.2}$$

Thus, when the mixing and dissipation length scales have not reached their threshold values (strong stratification and/or low TKE), TKE variations evenly impact the terms of the tendency (Figure A.12 (1)). The TKE production is then triggered by strong vertical shear relative to the stratification, i.e. when the bulk Richardson number R_i decreases below $R_{i_c} \simeq 0.23$ (Equation A.2). On the other hand, when the mixing and dissipation length scales reach their threshold values (weak stratification and/or great TKE), they become disconnected from the TKE, which becomes a net source of dissipation (Figure A.12 (2)). The TKE production then requires strong vertical shear of horizontal currents and low stratification relative to the TKE (Equation A.1).

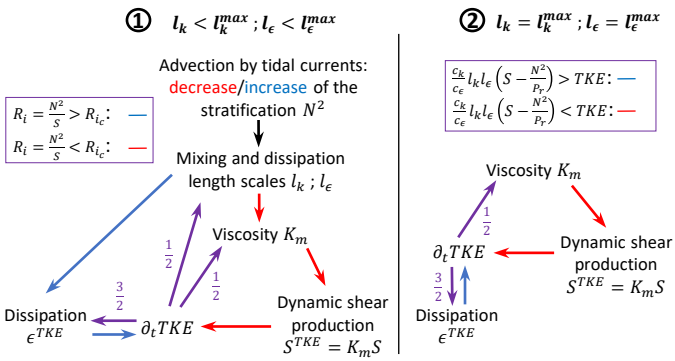

Figure A.12: Conceptual diagram of the mechanisms controlling TKE production and destruction. On the left (1) behavior of the TKE tendency in the presence of strong stratification and/or low TKE. On the right (2) behavior of the TKE tendency in the presence of weak stratification and/or high TKE. Red and blue arrows denote positive and negative feedback, respectively. When tidal currents reduce the stratification, the black arrow represents the positive feedback on the mixing and dissipation length scales; otherwise, it represents negative feedback. Purple arrows represent either positive or negative feedback. The conditions in the purple frame define their color. R_i refers to the bulk Richardson number, the ratio between stratification and vertical shear of zonal currents. $R_{i_c} \simeq 0.23$ is a bulk Richardson critical value. $Pr = min(10, max(1, 5 * R_i))$ refers to the Prandtl number. The number next to the purple arrows represents the order of the TKE in the other terms. We do not represent the buoyancy flux in the diagram, but we consider it in the conditions for the production or destruction of TKE.

Appendix B. Overview of the horizontal buoyancy flux at hourly frequency

This appendix provides an overview of the diapycnal mixing produced by the horizontal buoyancy flux $|K_h M^2| = K_h \sqrt{(\partial_x^2 \rho)^2 + (\partial_y^2 \rho)^2}$ during the period analysed in section 3.4 “Tidal Recirculation Patterns”, that is January 8, 1981, 1:00 p.m. - 11:00 p.m.. The pseudo-meridional average of $|K_h M^2|$ during this period is displayed in Figure B.13. First, it is important to note that although $|K_h M^2|$ is higher than

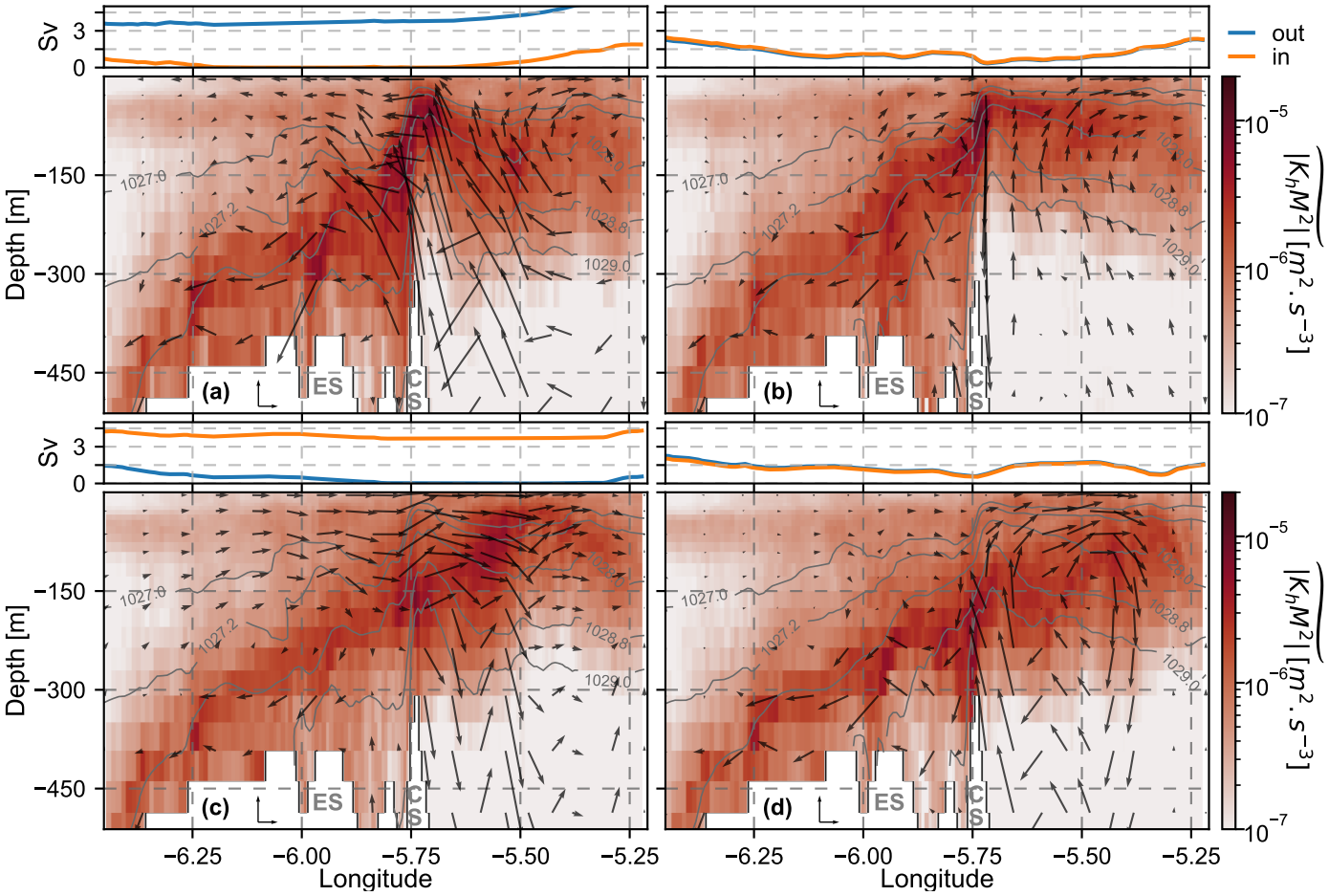

Figure B.13: Pseudo-meridional average of horizontal buoyancy fluxes $|K_h M^2| = K_h \sqrt{(\partial_x^2 \rho)^2 + (\partial_y^2 \rho)^2}$, with $K_h = 2\text{m}^2.\text{s}^{-1}$ the horizontal Laplacian diffusivity coefficient. The fields are hourly outputs, extracted on 1981/01/08 at 1 p.m. (1), 4 p.m. (2), 7 p.m. (3) and 10 p.m. (4) (black dots in Figure 7). The top blue and orange line plots represent the westward and eastward volume transport (in Sverdrups), respectively, computed from hourly outputs of zonal velocity. The 1027kg.m^{-3},1027.2kg.m^{-3}, 1028kg.m^{-3}, 1028.8kg.m^{-3}, 1029kg.m^{-3} isopycnal surfaces are illustrated in contours for all panels. The acronyms "ES" and "CS" in gray refer to the Espartel Sill and the Camarinal Sill, respectively (see Figure 1). Spatial averages are performed as detailed in Figure 5.

$|B|$ (Figures 9 and 10, panels (b)), it powers a less intense diapycnal mixing. Indeed, over the domain represented in Figure 1, $\int |\nabla \cdot K_h M^2| \, dV$ is, on average, five-time inferior to $\int |\partial_z B| \, dV$ during the period considered in Figure B.13. With that in mind, $|K_h M^2|$ provides meaningful information about the location and intensity of the diapycnal mixing powered by the horizontal eddy diffusivity. Unlike $|B|$, which is mainly intensified within the Atlantic and Mediterranean layers, $|K_h M^2|$ is more homogeneous and reaches its maximum at the interface between the Atlantic and Mediterranean layers. More specifically, over the period analyzed, $|K_h M^2|$ is high between the 1029 - 1027 kg.m^{-3} isopycnals, which are sheared by tidal circulation patterns. Thus, the absolute horizontal buoyancy flux can be considered a less intense but complementary source of diapycnal mixing at the SoG.

Appendix C. Vertical shear and stratification variations along the tidal cycle

In this appendix, we provide additional or supporting information for section 3.4 "Tidal Recirculation Patterns". More specifically, we outline the variations of the vertical shear of horizontal currents Sh and the vertical stratification N^2 along the tidal cycle on January 8, 1981, and provide insights into the mechanism driving N^2 variations.

Regarding the vertical shear variation ΔSh, displayed in the panels (a) of Figures C.14 and C.15, above the seafloor, it is mainly consistent with the intensification or weakening of the Mediterranean outflow, except at the CS and ES, where tidal reticulation patterns influence Sh. In the Atlantic layer, ΔSh is more complex to interpret. However, it provides insights into the influence of the eastward internal bore released at the CS, which mainly intensifies Sh along its trail (Figure C.15). Stratification variations, displayed in panels (b) of Figures C.14 and C.15, are organized in dipoles, reflecting, on the one hand, a stretching of the isopycnals ($\Delta N^2 < 0$), and on the other hand,

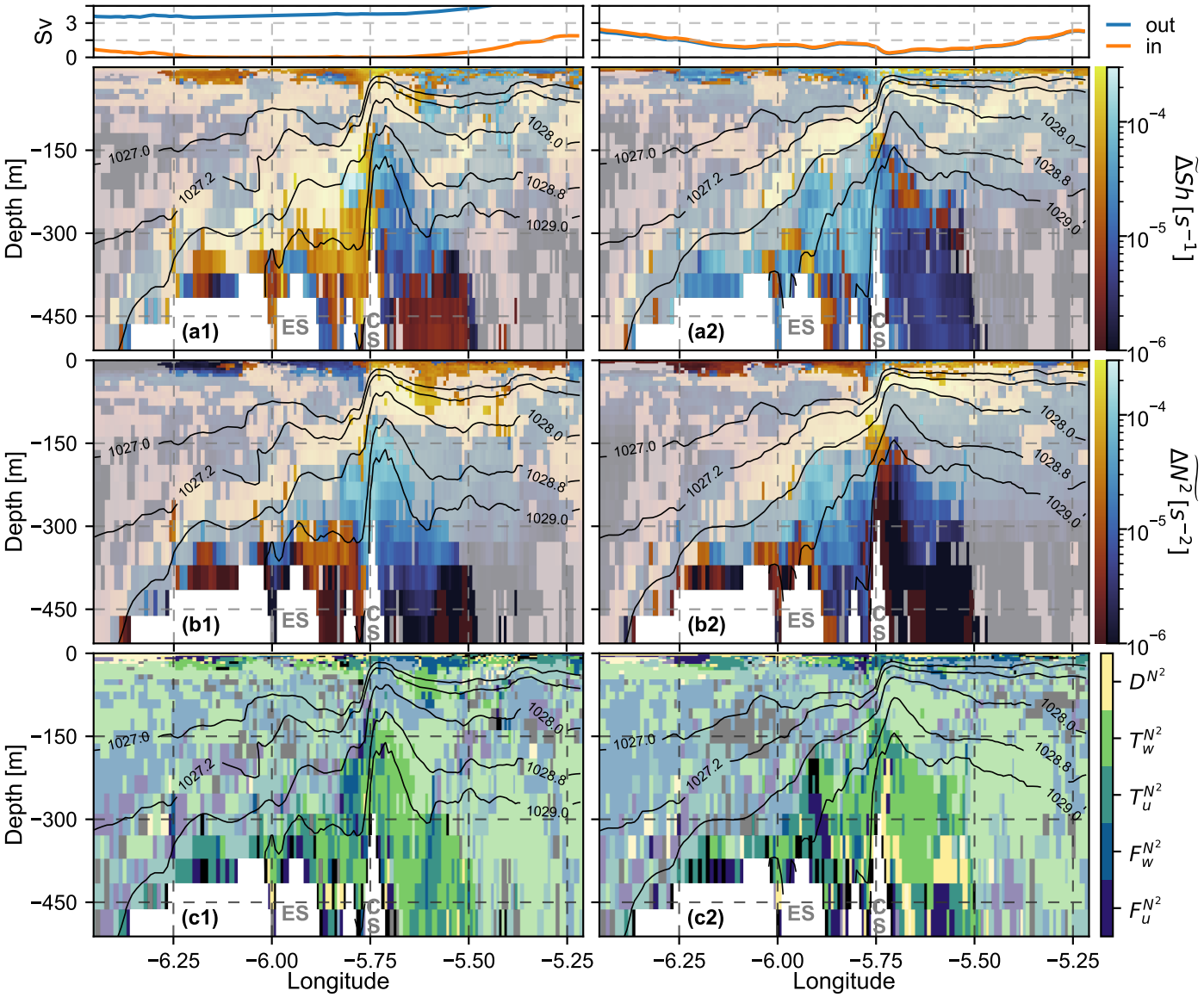

Figure C.14: In shades, from top to bottom: (a) pseudo-meridional average of vertical shear (Sh) and (b) stratification (N^2) variation with respect to the previous tidal phase, and (c) processes dominating the stratification tendency (the term with the maximum absolute value). In panels (c), the considered mechanisms are turbulent buoyancy diffusion (D^{N^2}), vertical and zonal advection of stratification ($T_W^{N^2}$ and $T_U^{N^2}$, respectively), vertical and zonal frontogenesis ($F_W^{N^2}$ and $F_U^{N^2}$, respectively). For the sake of readability, we shade the areas where other mechanisms drive the stratification tendency in black. The fields are hourly outputs, extracted on 1981/01/08 at 1 p.m. (1), 4 p.m. (2) (black dots in Figure 7). The top blue and orange line plots represent the westward and eastward volume transport (in Sverdrups), respectively, computed from hourly outputs of zonal velocity. The 1027kg.m^{-3},1027.2kg.m^{-3}, 1028kg.m^{-3}, 1028.8kg.m^{-3}, 1029kg.m^{-3} isopycnal surfaces are illustrated in contours for all panels. Areas where the absolute buoyancy flux variations are lower than 2.5 10^{-8} m^2.s^{-4} in absolute value are made transparent to make the figure clearer. The acronyms "ES" and "CS" in gray refer to the Espartel Sill and the Camarinal Sill, respectively (see Figure 1). Spatial averages of the vertical shear and stratification are performed as detailed in Figure 5 considering only the cells driving the mean meridional variation computed as described in Appendix D.

a squashing of the isopycnals ($\Delta N^2 > 0$). In panels (c), we indicate the mechanism that contributes the most to the mean stratification tendency based on the vertical stratification tendency equation (see Appendix E for the full derivation). Three processes are involved in this tendency: turbulent buoyancy diffusion (D^{N^2}), frontogenesis (F^{N^2}), and advection of stratification (T^{N^2}). Strong tendencies are mainly due to vertical or zonal advection. For weaker tendencies, the balance is mitigated as zonal and vertical frontogenesis can locally dominate. Finally, turbulent buoyancy diffusion, meridional frontogenesis, and meridional advection play a minor role (the two latter are not displayed in Figures C.14 and C.15).

Appendix D. On the diagnostic of buoyancy flux variations

This appendix details the method used to diagnose the mechanisms driving absolute buoyancy flux ($|B| = |K_t N^2|$) variations at the SoG. The method mainly relies on the straightforward influence of stratification and vertical shear on the production of TKE (Appendix A). Namely, the production of TKE increases

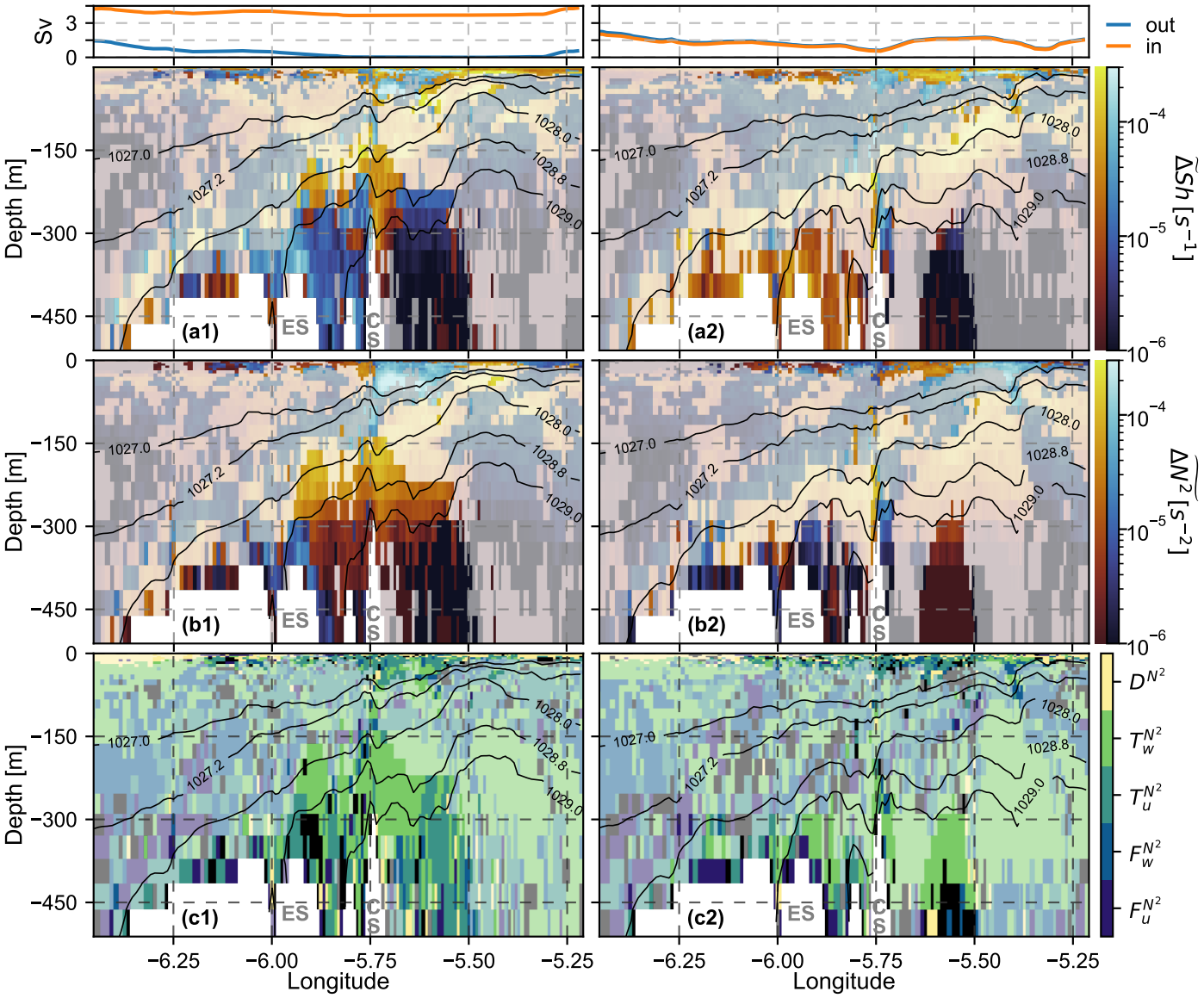

Figure C.15: Same as Figure C.14 for hourly outputs extracted at 7 p.m. (1) and 10 p.m. (2) (black dots in Figure 7).

as stratification weakens and vertical shear intensifies. However, to extend this simple reasoning to $|B|$, we must first verify that the TKE tendency drives its tendency. Since the buoyancy flux has a limited influence on the TKE at the SoG (see section 3.3), we can have a qualitative idea of the hypothesis validity by comparing meridionally consistent patterns of TKE and $|B|$ variations. To do so, we use the following cost function:

$$J(x) = C + \text{sign}(x)\log_{10}(x) \tag{D.1}$$

with C a given constant, representing the lowest order of magnitude to be considered for x, and sign(x) the sign function; sign(x) = 1 if $x > 0$; sign(x) = -1 otherwise.
We choose this specific cost function for its consistency to exponential variations and linear behavior near zero, provided that the constant C is correctly defined. In the following, we use $C = 10^{-8}$ s^{-2} for N^2, $C = 10^{-15}$ m^2.s^{-3} for B, $C = 10^{-12}$ m^2.s^{-2} for TKE, and $C = 10^{-8}$ s^{-1} for the vertical shear of horizontal currents Sh. These values are set to have a minimal impact when applying the function to a set of positive values.

To validate the hypothesis formulated above, we first compute the meridional average of $f(\Delta|B|)$, where $\Delta|B|$ is the variation of absolute buoyancy flux with respect to a previous state 3 hours earlier. We consider that a 3-hour time gap is sufficiently small to follow the variations of vertical shear and stratification and sufficiently long to minimize the diagnostic sensitivity to short-scale and transient variations. Thus, for each of the meridional profiles considered, the average $f(\Delta|B|)$ indicates whether $|B|$ consistently increases or decreases. In the following, in order to isolate the mechanism driving meridionally consistent variations of $|B|$, we only consider the cells responsible for these variations. For each meridional profile, we average the image of $|B|$ and TKE variation by the cost

function over these cells. Over the analyzed period, the resulting fields are highly correlated (Pearson correlation coefficients between 0.94 and 0.96) over the ocean interior, illustrating a strong relationship between $|B|$ and TKE tendencies. We do not consider the top fifty meters and the cells directly above the seafloor in this analysis because boundary conditions influence the intensity of ΔB in these areas, which may disturb the correlation scores. However, note that the influence of boundary conditions is not an issue in the following as vertical shear variations indirectly reflect it. Thus, we conclude that the buoyancy flux variations are, at least to the first order, resulting from TKE variation.

In light of these results, we consider it reasonable to interpret the variation of $|B|$ using simple logical relations based on the effects of stratification and vertical shear on the TKE tendency. Theses logical relations, summarized in table D.2, are applied to the meridional averages of $f(\Delta|B|)$ (panels (c) of the Figures 9, 10), $f(\Delta|N^2|)$ and $f(\Delta|\mathrm{Sh}|)$ (panels (a) and (b) of the Figures C.14 and C.15) over the cells responsible for the meridionally consistent variations of $|B|$. When both stratification and vertical shear drive $|B|$, we identify the dominant mechanism by comparing the respective influence of their variation on the Richardson number $Ri = N^2/\mathrm{Sh}$. Namely, we compare the following terms: $\frac{\Delta N^2}{\mathrm{Sh}}$ and $\frac{\Delta \mathrm{Sh} N^2}{\mathrm{Sh}(\mathrm{Sh}+\Delta \mathrm{Sh})}$. Finally, note that the cases marked as N.A. in Table D.2 should never occur if the variations of $|B|$ are fully defined by the TKE tendency. In practice, these cases are encountered at a few locations, shaded in black in Figures 9 and 10, where the formulated hypothesis fails. However, the few occurrences of these exceptions gives confidence in the consistency of the diagnostics.

(a) $\Delta|B| > 0$

	$\Delta \mathrm{Sh} > 0$	$\Delta \mathrm{Sh} < 0$
$\Delta N^2 > 0$	Sh	N.A
$\Delta N^2 < 0$	both	N^2

(b) $\Delta|B| < 0$

	$\Delta \mathrm{Sh} > 0$	$\Delta \mathrm{Sh} < 0$
$\Delta N^2 > 0$	N^2	both
$\Delta N^2 < 0$	N.A	Sh

Table D.2: These tables summarize, for a given variation of the absolute buoyancy flux $|B|$, the possible variations of vertical shear of horizontal currents (Sh) and stratification (N^2) and the driving mechanism that may be deduced from these combinations. In a nutshell, the buoyancy flux is supposed, as for the TKE, to increase when vertical shear intensifies and stratification weakens. The driving mechanism is diagnosed as the one of consistent variations with respect to the buoyancy flux. The acronym N.A. (Not Attributed) indicates combinations not allowed by the theoretical framework. We indicate the cases where both stratification and vertical shear drive the buoyancy flux tendency with the term "both".

Appendix E. Derivation of the stratification tendency

In this appendix, we formulate the tendency equation for the vertical density stratification. As in Hoskins (1982), we start from the Lagrangian trend of density which we then derive vertically:

$$\begin{aligned} \frac{d\rho}{dt} &= \frac{\partial \rho}{\partial t} + \mathbf{U}\cdot\nabla\rho \\ \Rightarrow \frac{\partial}{\partial z}\left(\frac{d\rho}{dt}\right) &= \frac{\partial^2 \rho}{\partial z \partial t} + \frac{\partial \mathbf{U}}{\partial z}\cdot\nabla\rho + \mathbf{U}\cdot\nabla\frac{\partial \rho}{\partial z} \\ \Rightarrow \frac{\partial}{\partial z}\left(\frac{d\rho}{dt}\right) &= \frac{d}{dt}\left(\frac{\partial \rho}{\partial z}\right) + \frac{\partial \mathbf{U}}{\partial z}\cdot\nabla\rho \end{aligned} \tag{E.1}$$

With $\mathbf{U} = (u, v, w)$ the velocity vector and ∇ the nabla operator.

Assuming that the Lagrangian tendency of potential density is dominated by turbulent mixing, i.e. $\frac{d\rho}{dt} \simeq -\frac{\partial}{\partial z}\left(K_t \frac{\partial \rho}{\partial z}\right)$, we can write :

$$\begin{aligned} \frac{d}{dt}\left(\frac{\partial \rho}{\partial z}\right) &\simeq -\frac{\partial^2}{\partial z^2}\left(K_t \frac{\partial \rho}{\partial z}\right) - \frac{\partial \mathbf{U}}{\partial z}\cdot\nabla\rho \\ \Rightarrow \frac{\partial}{\partial t}\left(\frac{\partial \rho}{\partial z}\right) &\simeq -\frac{\partial^2}{\partial z^2}\left(K_t \frac{\partial \rho}{\partial z}\right) - \frac{\partial \mathbf{U}}{\partial z}\cdot\nabla\rho - \mathbf{U}\cdot\nabla\frac{\partial \rho}{\partial z} \end{aligned} \tag{E.2}$$

From the definition of the Brunt-Väisälä frequency : $N^2 = -\frac{g}{\rho_0}\frac{\partial \rho}{\partial z}$ we can thus estimate the vertical stratification Eulerian tendency as follows:

$$\frac{\partial N^2}{\partial t} \simeq \underbrace{-\frac{\partial^2 B}{\partial z^2}}_{D^{N^2}} + \underbrace{\frac{g}{\rho_0}\frac{\partial \mathbf{U}}{\partial z}\cdot\nabla\rho}_{F_u^{N^2}+F_v^{N^2}+F_w^{N^2}} - \underbrace{\mathbf{U}\cdot\nabla N^2}_{T_u^{N^2}+T_v^{N^2}+T_w^{N^2}} \tag{E.3}$$

with $B = K_t N^2$ the vertical buoyancy flux. This tendency is composed of 7 terms, which can be associated with three mechanisms:

- The turbulent diffusion of vertical stratification D^{N^2}
- The frontogenesis terms, which represent the deformation of density gradients by convergent/divergent velocities: $F_u^{N^2}$,$F_v^{N^2}$, and $F_w^{N^2}$.
- The transport of vertical stratification: zonal $T_u^{N^2}$, meridional $T_v^{N^2}$ and vertical $T_w^{N^2}$. It simply advects the N^2 field.

To validate the estimated density tendency, for each hour illustrated in Figures 9 and 10, we have compared the sum of the tendency terms computed from 2 hourly averaged fields with a first-order finite-difference 3-hourly spaced upwind scheme estimate of the total tendency. The error in the total density tendency decimal logarithm is lower than 10% over at least 97% of the domain and low in areas of strong tendency.

References

Adcroft, A., Campin, J.M., 2004. Rescaled height coordinates for accurate representation of free-surface flows in ocean circulation models. Ocean Modelling 7, 269–284. URL: https://linkinghub.elsevier.com/retrieve/pii/S1463500303000544, doi:10.1016/j.ocemod.2003.09.003.

Adcroft, A., Hill, C., Marshall, J., 1997. Representation of topography by shaved cells in a height coordinate ocean model. Monthly Weather Review 125, 2293–2315. URL: http://journals.ametsoc.org/doi/10.1175/1520-0493(1997)125%3C2293:ROTBSC%3E2.0.CO;2, doi:10.1175/1520-0493(1997)125<2293:ROTBSC>2.0.CO;2.

Álvarez, , Izquierdo, A., González, C.J., Bruno, M., Mañanes, R., 2019. Some considerations about non-hydrostatic vs. hydrostatic simulation of short-period internal waves. A case study: The Strait of Gibraltar. Continental Shelf Research 181, 174–186. URL: https://doi.org/10.1016/j.csr.2019.05.016https://linkinghub.elsevier.com/retrieve/pii/S0278434318303236, doi:10.1016/j.csr.2019.05.016.

Baschek, B., Send, U., Lafuente, J.G., Candela, J., 2001. Transport estimates in the Strait of Gibraltar with a tidal inverse model. Journal of Geophysical Research: Oceans 106, 31033–31044. doi:10.1029/2000jc000458.

Bignami, F., Marullo, S., Santoleri, R., Schiano, M.E., 1995. Longwave radiation budget in the Mediterranean Sea. Journal of Geophysical Research 100, 2501–2514. doi:10.1029/94JC02496.

Bouffard, D., Boegman, L., 2013. A diapycnal diffusivity model for stratified environmental flows. Dynamics of Atmospheres and Oceans 61-62, 14–34. URL: http://dx.doi.org/10.1016/j.dynatmoce.2013.02.002, doi:10.1016/j.dynatmoce.2013.02.002.

Bougeault, P., Andre, J.C., 1986. On the stability of the third-order turbulence closure for the modeling of the stratocumulus-topped boundary layer. Journal of the Atmospheric Sciences 43, 1574–1581. doi:10.1175/1520-0469(1986)043<1574:OTSOTT>2.0.CO;2.

Bougeault, P., Lacarrere, P., 1989. Parameterization of orography-induced turbulence in a mesobeta-scale model. doi:10.1175/1520-0493(1989)117<1872:POOITI>2.0.CO;2.

Boutov, D., Peliz, , Miranda, P.M., Soares, P.M., Cardoso, R.M., Prieto, L., Ruiz, J., García-Lafuente, J., 2014. Inter-annual variability and long term predictability of exchanges through the Strait of Gibraltar. Global and Planetary Change 114, 23–37. URL: http://dx.doi.org/10.1016/j.gloplacha.2013.12.009, doi:10.1016/j.gloplacha.2013.12.009.

Brandt, P., Alpers, W., Backhaus, J.O., 1996. Study of the generation and propagation of internal waves in the Strait of Gibraltar using a numerical model and synthetic aperture radar images of the European ERS 1 satellite. Journal of Geophysical Research: Oceans 101, 14237–14252. URL: http://doi.wiley.com/10.1029/96JC00540, doi:10.1029/96JC00540.

Bray, N.A., Ochoa, J., Kinder, T.H., 1995. The role of the interface in exchange through the Strait of Gibraltar. Journal of Geophysical Research 100. doi:10.1029/95jc00381.

Bruno, M., Chioua, J., Romero, J., Vázquez, A., Macías, D., Dastis, C., Ramírez-Romero, E., Echevarria, F., Reyes, J., García, C., 2013. The importance of sub-mesoscale processes for the exchange of properties through the Strait of Gibraltar. Progress in Oceanography 116, 66–79. URL: https://linkinghub.elsevier.com/retrieve/pii/S0079661113000943, doi:10.1016/j.pocean.2013.06.006.

Bryden, H., Stommel, H., 1984. Limiting processes that determine basic features of the circulation in the Mediterranean Sea. Oceanologica acta 7, 289–296.

Bryden, H.L., Candela, J., Kinder, T.H., 1994. Exchange through the Strait of Gibraltar. Progress in Oceanography 33, 201–248. doi:10.1016/0079-6611(94)90028-0.

Bryden, H.L., Kinder, T.H., 1986. Gibraltar experiment : a plan for dynamic and kinematic investigations of strait mixing, exchange and turbulence. Woods Hole Oceanographic Institution, Woods Hole, MA. URL: https://hdl.handle.net/1912/7955, doi:10.1575/1912/7955.

Campin, J.M., Adcroft, A., Hill, C., Marshall, J., 2004. Conservation of properties in a free-surface model. Ocean Modelling 6, 221–244. URL: https://linkinghub.elsevier.com/retrieve/pii/S146350030300009X, doi:10.1016/S1463-5003(03)00009-X.

Candela, J., Winant, C., Ruiz, A., 1990. Tides in the strait of gibraltar. Journal of Geophysical Research 95, 7313–7335. doi:10.1029/JC095iC05p07313.

Egbert, G.D., Erofeeva, S.Y., 2002. Efficient inverse modeling of barotropic ocean tides. Journal of Atmospheric and Oceanic Technology 19, 183–204. doi:10.1175/1520-0426(2002)019<0183:EIMOBO>2.0.CO;2.

Farmer, D.M., Armi, L., 1985. The internal hydraulics of the Strait of Gibraltar and associated sills and narrows. Oceanologica acta 8, 37–46. URL: https://archimer.ifremer.fr/doc/00112/22325/.

Farmer, D.M., Armi, L., Armi, L., Farmer, D.M., 1988. The flow of Atlantic water through the Strait of Gibraltar. Progress in Oceanography 21, 1. URL: https://doi.org/10.1016/0079-6611(88)90055-9, doi:10.1016/0079-6611(88)90055-9.

Fernando, H.J., 1991. Turbulent mixing in stratified fluids. Annual Review of Fluid Mechanics 23, 455–493. doi:10.1146/annurev.fl.23.010191.002323.

Ferrarin, C., Bellafiore, D., Sannino, G., Bajo, M., Umgiesser, G., 2018. Tidal dynamics in the inter-connected Mediterranean, Marmara, Black and Azov seas. Progress in Oceanography 161, 102–115. doi:10.1016/j.pocean.2018.02.006.

Foreman, M.G., 1977. Manual for Tidal Heights And Prediction. Pac. Mar. Sci. Rep. 77–10.

García Lafuente, J., Álvarez Fanjul, E., Vargas, J.M., Ratsimandresey, A.W., 2002. Subinertial variability in the flow through the Strait of Gibraltar. Journal of Geophysical Research: Oceans 107, 3168. URL: http://doi.wiley.com/10.1029/2001JC001104, doi:10.1029/2001jc001104.

García Lafuente, J., Bruque Pozas, E., Sánchez Garrido, J.C., Sannino, G., Sammartino, S., 2013. The interface mixing layer and the tidal dynamics at the eastern part of the Strait of Gibraltar. Journal of Marine Systems 117-118, 31–42. URL: http://dx.doi.org/10.1016/j.jmarsys.2013.02.014, doi:10.1016/j.jmarsys.2013.02.014.

Gaspar, P., Grégoris, Y., Lefevre, J.M., 1990. A simple eddy kinetic energy model for simulations of the oceanic vertical mixing: Tests at station Papa and long-term upper ocean study site. Journal of Geophysical Research 95, 16179. doi:10.1029/jc095ic09p16179.

Giorgi, F., Jones, C., Asrar, G., 2009. Addressing climate information needs at the regional level: the CORDEX framework. ... Organization (WMO) Bulletin 58, 175–183. URL: http://www.euro-cordex.net/uploads/media/Download_01.pdf.

Gökaşan, E., Ergin, M., Özyalvaç, M., Sur, H.I., Tur, H., Görüm, T., Ustaömer, T., Batuk, F.G., Alp, H., Birkan, H., Türker, A., Gezgin, E., Özturan, M., 2007. Factors controlling the morphological evolution of the Çanakkale Strait (Dardanelles, Turkey). Geo-Marine Letters 28, 107–129. doi:10.1007/s00367-007-0094-y.

Gökaşan, E., Tur, H., Ecevitoğlu, B., Görüm, T., Türker, A., Tok, B., Çağlak, F., Birkan, H., Şimşek, M., 2005. Evidence and implications of massive erosion along the Strait of Istanbul (Bosphorus). Geo-Marine Letters 25, 324–342. doi:10.1007/s00367-005-0216-3.

Harzallah, A., Alioua, M., Li, L., 2014. Mass exchange at the Strait of Gibraltar in response to tidal and lower frequency forcing as simulated by a Mediterranean Sea model. Tellus A: Dynamic Meteorology and Oceanography 66, 23871. URL: https://doi.org/10.3402/tellusa.v66.23871, doi:10.3402/tellusa.v66.23871.

Harzallah, A., Jordà, G., Dubois, C., Sannino, G., Carillo, A., Li, L., Arsouze, T., Cavicchia, L., Beuvier, J., Akhtar, N., 2018. Long term evolution of heat budget in the Mediterranean Sea from Med-CORDEX forced and coupled simulations. Climate Dynamics 51, 1145–1165. doi:10.1007/s00382-016-3363-5.

Hilt, M., Auclair, F., Benshila, R., Bordois, L., Capet, X., Debreu, L., Dumas, F., Jullien, S., Lemarié, F., Marchesiello, P., Nguyen, C., Roblou, L., 2020. Numerical modelling of hydraulic control, solitary waves and primary instabilities in the Strait of Gibraltar. Ocean Modelling 151, 101642. URL: https://linkinghub.elsevier.com/retrieve/pii/S146350032030144X, doi:10.1016/j.ocemod.2020.101642.

Hoskins, J.B., 1982. The mathematical theory of frontogenesis. in: Annual Review of Fluid Mechanics 14 , M. Va, 131–151. URL: https://doi.org/10.1146/annurev.fl.14.010182.001023, doi:10.1146/annurev.fl.14.010182.001023.

Huertas, I.E., Ríos, A.F., García-Lafuente, J., Navarro, G., Makaoui, A., Snchez-Romn, A., Rodriguez-Galvez, S., Orbi, A., Ruíz, J., Pérez, F.F., 2012. Atlantic forcing of the Mediterranean oligotrophy. Global Biogeochemical Cycles 26, 1–9. doi:10.1029/2011GB004167.

Jackett, D.R., Mcdougall, T.J., 1995. Minimal Adjustment of Hydrographic Profiles to Achieve Static Stability. Journal of Atmospheric and Oceanic Technology 12, 381–389. doi:10.1175/1520-0426(1995)012<0381:maohpt>2.0.co;2.

Jackson, P.R., Rehmann, C.R., 2014. Experiments on differential scalar mixing in turbulence in a sheared, stratified flow. Journal of Physical Oceanography 44, 2661–2680. doi:10.1175/JPO-D-14-0027.1.

Jordà, G., Von Schuckmann, K., Josey, S.A., Caniaux, G., García-Lafuente, J., Sammartino, S., Özsoy, E., Polcher, J., Notarstefano, G., Poulain, P.M.,

Adloff, F., Salat, J., Naranjo, C., Schroeder, K., Chiggiato, J., Sannino, G., Macías, D., 2017. The Mediterranean Sea heat and mass budgets: Estimates, uncertainties and perspectives. Progress in Oceanography 156, 174–208. doi:10.1016/j.pocean.2017.07.001.

Kinder, T.H., Bryden, H.L., 1990. Aspiration of Deep Waters through Straits, in: Pratt, L.J. (Ed.), The Physical Oceanography of Sea Straits. Springer Netherlands, Dordrecht, pp. 295–319. URL: https://doi.org/10.1007/978-94-009-0677-8_14, doi:10.1007/978-94-009-0677-8{_}14.

Kolmogorov, A.N., 1942. Equations of turbulent motion in an incompressible fluid. Dokl. Akad. Nauk SSSR , 56–58.

Lacombe, H., Richez, C., 1982. The regime of the strait of gibraltar. Elsevier Oceanography Series 34, 13–73. doi:10.1016/S0422-9894(08)71237-6.

Lafuente, J.G., Almazan, J.L., Castillejo, F., Khribeche, A., Hakimi, A., 1990. Sea level in the Strait of Gibraltar: tides. Int. Hydrographic Rev. 67, 111–125.

Lafuente, J.G., Vargas, J.M., Plaza, F., Sarhan, T., Candela, J., Bascheck, B., 2000. Tide at the eastern section of the Strait of Gibraltar. Journal of Geophysical Research: Oceans 105, 14197–14213. doi:10.1029/2000jc900007.

Lahaye, N., Gula, J., Roullet, G., 2020. Internal Tide Cycle and Topographic Scattering Over the North Mid-Atlantic Ridge. Journal of Geophysical Research: Oceans 125, 1–21. URL: https://onlinelibrary.wiley.com/doi/10.1029/2020JC016376, doi:10.1029/2020JC016376.

Large, W.G., Yeager, S.G., 2004. Diurnal to decadal global forcing for ocean and sea-ice models: The data sets and flux climatologies. NCAR Tech. Note TN–460+ST, 105pp. doi:10.5065/D6KK98Q6.

de Lavergne, C., Madec, G., Le Sommer, J., Nurser, A.J.G., Naveira Garabato, A.C., 2016. The Impact of a Variable Mixing Efficiency on the Abyssal Overturning. Journal of Physical Oceanography 46, 663–681. URL: https://journals.ametsoc.org/view/journals/phoc/46/2/jpo-d-14-0259.1.xml, doi:10.1175/JPO-D-14-0259.1.

de Lavergne, C., Vic, C., Madec, G., Roquet, F., Waterhouse, A.F., Whalen, C.B., Cuypers, Y., Bouruet-Aubertot, P., Ferron, B., Hibiya, T., 2020. A Parameterization of Local and Remote Tidal Mixing. Journal of Advances in Modeling Earth Systems 12. URL: https://doi.org/10.1029/2020MS002065, doi:10.1029/2020MS002065.

Llasses, J., Jordà, G., Gomis, D., Adloff, F., Macías, D., Harzallah, A., Arsouze, T., Akthar, N., Li, L., Elizalde, A., Sannino, G., 2018. Heat and salt redistribution within the Mediterranean Sea in the Med-CORDEX model ensemble. Climate Dynamics 51, 1119–1143. doi:10.1007/s00382-016-3242-0.

Macias, D., García, C.M., Echevarría Navas, F., Vázquez-López-Escobar, A., Bruno Mejías, M., 2006. Tidal induced variability of mixing processes on Camarinal Sill (Strait of Gibraltar): A pulsating event. Journal of Marine Systems 60, 177–192. URL: https://linkinghub.elsevier.com/retrieve/pii/S0924796305002095, doi:10.1016/j.jmarsys.2005.12.003.

Marshall, J., Adcroft, A., Hill, C., Perelman, L., Heisey, C., 1997a. A finite-volume, incompressible navier stokes model for, studies of the ocean on parallel computers. Journal of Geophysical Research C: Oceans 102, 5753–5766. doi:10.1029/96JC02775.

Marshall, J., Hill, C., Perelman, L., Adcroft, A., 1997b. Hydrostatic, quasi-hydrostatic, and nonhydrostatic ocean modeling. Journal of Geophysical Research C: Oceans 102, 5733–5752. doi:10.1029/96JC02776.

Morozov, E.G., Trulsen, K., Velarde, M.G., Vlasenko, V.I., 2002. Internal tides in the Strait of Gibraltar. Journal of Physical Oceanography 32, 3193–3206. URL: http://journals.ametsoc.org/doi/10.1175/1520-0485(2002)032%3C3193:ITITSO%3E2.0.CO;2, doi:10.1175/1520-0485(2002)032<3193:ITITSO>2.0.CO;2.

Naranjo, C., Garcia-Lafuente, J., Sannino, G., Sanchez-Garrido, J.C., 2014. How much do tides affect the circulation of the Mediterranean Sea? From local processes in the Strait of Gibraltar to basin-scale effects. Progress in Oceanography 127, 108–116. doi:10.1016/j.pocean.2014.06.005.

Osborn, T.R., 1980. Estimates of the Local Rate of Vertical Diffusion from Dissipation Measurements. Journal of Physical Oceanography 10, 83–89. URL: https://doi.org/10.1175/1520-0485(1980)010%3C0083:EOTLRO%3E2.0.CO;2, doi:10.1175/1520-0485(1980)010<0083:eotlro>2.0.co;2.

Palma, M., Iacono, R., Sannino, G., Bargagli, A., Carillo, A., Fekete, B.M., Lombardi, E., Napolitano, E., Pisacane, G., Struglia, M.V., 2020. Short-term, linear, and non-linear local effects of the tides on the surface dynamics in a new, high-resolution model of the Mediterranean Sea circulation. Ocean Dynamics 70, 935–963. doi:10.1007/s10236-020-01364-6.

Parras-Berrocal, I.M., Vázquez, R., Cabos, W., Sein, D.V., Álvarez, O., Bruno, M., Izquierdo, A., 2022. Surface and Intermediate Water Changes Triggering the Future Collapse of Deep Water Formation in the North Western Mediterranean. Geophysical Research Letters 49, 1–10. URL: https://onlinelibrary.wiley.com/doi/10.1029/2021GL095404, doi:10.1029/2021GL095404.

Pawlowicz, R., Beardsley, B., Lentz, S., 2002. Classical tidal harmonic analysis including error estimates in MATLAB using T_TIDE. Computers & Geosciences 28, 929–937. URL: https://linkinghub.elsevier.com/retrieve/pii/S0098300402000134, doi:10.1016/S0098-3004(02)00013-4.

Pettigrew, N.R., Hyde, R.A., 1990. The Structure of the Internal Bore in the Strait of Gibraltar and its Influence on the Atlantic Inflow, in: The Physical Oceanography of Sea Straits. Springer Netherlands, Dordrecht, pp. 493–508. URL: http://link.springer.com/10.1007/978-94-009-0677-8_24, doi:10.1007/978-94-009-0677-8{_}24.

Potter, R.A., Lozier, M.S., 2004. On the warming and salinification of the Mediterranean outflow waters in the North Atlantic. Geophysical Research Letters 31, 1–4. doi:10.1029/2003GL018161.

Prandtl, L., 1925. Report on investigation of developed turbulence 5, 136–139.

Ramírez-Romero, E., Macías, D., García, C.M., Bruno, M., 2014. Biogeochemical patterns in the Atlantic Inflow through the Strait of Gibraltar. Deep-Sea Research Part I: Oceanographic Research Papers 85, 88–100. URL: http://dx.doi.org/10.1016/j.dsr.2013.12.004, doi:10.1016/j.dsr.2013.12.004.

Richez, C., 1994. Airborne synthetic aperture radar tracking of internal waves in the Strait of Gibraltar. Progress in Oceanography 33, 93–159. URL: https://linkinghub.elsevier.com/retrieve/pii/0079661194900023X, doi:10.1016/0079-6611(94)90023-X.

Richon, C., Dutay, J.C., Bopp, L., Le Vu, B., Orr, J.C., Somot, S., Dulac, F., 2019. Biogeochemical response of the Mediterranean Sea to the transient SRES-A2 climate change scenario. Biogeosciences 16, 135–165. doi:10.5194/bg-16-135-2019.

Sammartino, S., García Lafuente, J., Naranjo, C., Sánchez Garrido, J.C., Sánchez Leal, R., Sánchez Román, A., 2015. Ten years of marine current measurements in Espartel Sill, Strait of Gibraltar. Journal of Geophysical Research: Oceans 120, 6309–6328. doi:10.1002/2014JC010674.

Sanchez-Garrido, J.C., Sannino, G., Liberti, L., García Lafuente, J., Pratt, L., 2011. Numerical modeling of three-dimensional stratified tidal flow over Camarinal Sill, Strait of Gibraltar. Journal of Geophysical Research: Oceans 116, 1–17. doi:10.1029/2011JC007093.

Sánchez-Román, A., Criado-Aldeanueva, F., García-Lafuente, J., Sánchez, J., 2008. Vertical structure of tidal currents over Espartel and Camarinal sills, Strait of Gibraltar. Journal of Marine Systems 74, 120–133. URL: http://dx.doi.org/10.1016/j.jmarsys.2007.11.007https://linkinghub.elsevier.com/retrieve/pii/S0924796307002333, doi:10.1016/j.jmarsys.2007.11.007.

Sánchez-Román, A., García-Lafuente, J., Delgado, J., Sánchez-Garrido, J.C., Naranjo, C., 2012. Spatial and temporal variability of tidal flow in the Strait of Gibraltar. Journal of Marine Systems 98-99, 9–17. URL: http://dx.doi.org/10.1016/j.jmarsys.2012.02.011, doi:10.1016/j.jmarsys.2012.02.011.

Sanchez-Roman, A., Jorda, G., Sannino, G., Gomis, D., 2018. Modelling study of transformations of the exchange flows along the Strait of Gibraltar. Ocean Science 14, 1547–1566. doi:10.5194/os-14-1547-2018.

Sánchez-Román, A., Sannino, G., García-Lafuente, J., Carillo, A., Criado-Aldeanueva, F., 2009. Transport estimates at the western section of the Strait of Gibraltar: A combined experimental and numerical modeling study. Journal of Geophysical Research: Oceans 114. doi:10.1029/2008JC005023.

Sannino, G., Bargagli, A., Artale, V., 2004. Numerical modeling of the semidiurnal tidal exchange through the Strait of Gibraltar. Journal of Geophysical Research C: Oceans 109. doi:10.1029/2003JC002057.

Sannino, G., Carillo, A., Artale, V., 2007. Three-layer view of transports and hydraulics in the Strait of Gibraltar: A three-dimensional model study. Journal of Geophysical Research: Oceans 112. doi:10.1029/2006JC003717.

Sannino, G., Carillo, A., Pisacane, G., Naranjo, C., 2015. On the relevance of tidal forcing in modelling the Mediterranean thermohaline circulation. Progress in Oceanography 134, 304–329. doi:10.1016/j.pocean.2015.

03.002.

Sannino, G., Carillo, A., Pratt, L., 2009. Hydraulic criticality of the exchange flow through the strait of Gibraltar. Journal of Physical Oceanography 39, 2779–2799. doi:10.1175/2009JPO4075.1.

Sannino, G., Garrido, J.C., Liberti, L., Pratt, L., 2014. Exchange Flow through the Strait of Gibraltar as Simulated by a σ-Coordinate Hydrostatic Model and a z-Coordinate Nonhydrostatic Model. The Mediterranean Sea: Temporal Variability and Spatial Patterns 9781118847, 25–50. doi:10.1002/9781118847572.ch3.

Sannino, G., Sözer, A., Özsoy, E., 2017. A high-resolution modelling study of the Turkish Straits System. volume 67. Ocean Dynamics. doi:10.1007/s10236-017-1039-2.

Sanz, J.L., Acosta Yepes, J., Esteras, M., Herranz, P., Palomo, C., Sandoval, N., 1991. Prospección geofísica del Estrecho de Gibraltar: resultados del programa Hércules (1980-1983). Publicaciones Especiales del Instituto Espanol de Oceanografia , 7–48.

Schober, P., Boer, C., Schwarte, L.A., 2018. Correlation Coefficients. Anesthesia & Analgesia 126, 1763–1768. URL: http://journals.lww.com/00000539-201805000-00050, doi:10.1213/ANE.0000000000002864.

Send, U., Baschek, B., 2001. Intensive shipboard observations of the flow through the Strait of Gibraltar. Journal of Geophysical Research: Oceans 106, 31017–31032. URL: http://doi.wiley.com/10.1029/2000JC000459, doi:10.1029/2000JC000459.

Somot, S., Sevault, F., Déqué, M., 2006. Transient climate change scenario simulation of the Mediterranean Sea for the twenty-first century using a high-resolution ocean circulation model. Climate Dynamics 27, 851–879. doi:10.1007/s00382-006-0167-z.

Soto-Navarro, J., Jordá, G., Amores, A., Cabos, W., Somot, S., Sevault, F., Macías, D., Djurdjevic, V., Sannino, G., Li, L., Sein, D., 2020. Evolution of Mediterranean Sea water properties under climate change scenarios in the Med-CORDEX ensemble. volume 54. doi:10.1007/s00382-019-05105-4.

Soto-Navarro, J., Somot, S., Sevault, F., Beuvier, J., Criado-Aldeanueva, F., García-Lafuente, J., Béranger, K., 2015. Evaluation of regional ocean circulation models for the Mediterranean Sea at the Strait of Gibraltar: volume transport and thermohaline properties of the outflow. Climate Dynamics 44, 1277–1292. doi:10.1007/s00382-014-2179-4.

Strandberg, G., Bärring, L., Hansson, U., Jansson, C., Jones, C., Kjellström, E., Michael Kolax, Marco Kupiainen, G., Nikulin, P.S., Wang, A.U., Shiyu, 2014. CORDEX scenarios for Europe from the Rossby Centre regional climate model RCA4. Rep. Meteorol. Climatol. 116, 1–84. URL: https://www.smhi.se/polopoly_fs/1.90273!/Menu/general/extGroup/attachmentColHold/mainCol1/file/RMK_116.pdf.

Struglia, M.V., Mariotti, A., Filograsso, A., 2004. River discharge into the Mediterranean sea: Climatology and aspects of the observed variability. Journal of Climate 17, 4740–4751. doi:10.1175/JCLI-3225.1.

Tsimplis, M.N., Proctor, R., Flather, R.A., 1995. A two-dimensional tidal model for the Mediterranean Sea. Journal of Geophysical Research 100. doi:10.1029/95jc01671.

Umlauf, L., Burchard, H., 2005. Second-order turbulence closure models for geophysical boundary layers. A review of recent work. Continental Shelf Research 25, 795–827. URL: https://linkinghub.elsevier.com/retrieve/pii/S0278434304003152, doi:10.1016/j.csr.2004.08.004.

Vargas, J.M., García-Lafuente, J., Candela, J., Sánchez, A.J., 2006. Fortnightly and monthly variability of the exchange through the Strait of Gibraltar. Progress in Oceanography 70, 466–485. doi:10.1016/j.pocean.2006.07.001.

Vázquez, A., Stashchuk, N., Vlasenko, V., Bruno, M., Izquierdo, A., Gallacher, P.C., 2006. Evidence of multimodal structure of the baroclinic tide in the Strait of Gibraltar. Geophysical Research Letters 33, L17605. URL: http://doi.wiley.com/10.1029/2006GL026806, doi:10.1029/2006GL026806.

Vlasenko, V., Sanchez Garrido, J.C., Stashchuk, N., Lafuente, J.G., Losada, M., 2009. Three-dimensional evolution of large-amplitude internal waves in the Strait of Gibraltar. Journal of Physical Oceanography 39, 2230–2246. doi:10.1175/2009JPO4007.1.

Watson, G., Robinson, I.S., 1990. A study of internal wave propagation in the Strait of Gibraltar using shore-based marine radar images. J. Physical Oceanography 20, 374–395. URL: http://journals.ametsoc.org/doi/10.1175/1520-0485(1990)020%3C0374:ASOIWP%3E2.0.CO;2, doi:10.1175/1520-0485(1990)020<0374:asoiwp>2.0.co;2.

Wesson, J.C., Gregg, M.C., 1988. Turbulent Dissipation in the Strait of Gibraltar and Associated Mixing, in: Elsevier Oceanography Series. volume 46, pp. 201–212. URL: https://linkinghub.elsevier.com/retrieve/pii/S0422989408705476, doi:10.1016/S0422-9894(08)70547-6.

Wesson, J.C., Gregg, M.C., 1994. Mixing at Camarinal Sill in the Strait of Gibraltar. Journal of Geophysical Research 99, 9847–9878. doi:10.1029/94JC00256.

Xu, Z., 2018. A note on interpreting tidal harmonic constants. Ocean Dynamics 68, 211–222. URL: http://link.springer.com/10.1007/s10236-017-1122-8, doi:10.1007/s10236-017-1122-8.

Ziegenbein, J., 1969. Short internal waves in the Strait of Gibraltar. Deep Sea Research and Oceanographic Abstracts 16, 479–487. URL: https://linkinghub.elsevier.com/retrieve/pii/0011747169900369, doi:10.1016/0011-7471(69)90036-9.

Ziegenbein, J., 1970. Spatial observations of short internal waves in the Strait of Gibraltar. Deep-Sea Research and Oceanographic Abstracts 17, 867–875. URL: https://linkinghub.elsevier.com/retrieve/pii/0011747170900045, doi:10.1016/0011-7471(70)90004-5.